

Creation of an Fe_3P Schreibersite Density Functional Tight Binding Model for Astrobiological Simulations

Riccardo Dettori^{*,†,‡} and Nir Goldman^{*,†,¶}

[†]*Physical and Life Sciences Directorate, Lawrence Livermore National Laboratory, 7000 East Avenue, Livermore, California 94550, United States*

[‡]*Department of Physics, University of Cagliari, Monserrato, CA, 09042 Italy*

[¶]*Department of Chemical Engineering, University of California, Davis, California 95616, United States*

E-mail: riccardo.dettori@dsf.unica.it; ngoldman@lbl.gov

Abstract

The mineral schreibersite, e.g., Fe_3P , is commonly found in iron-rich meteorites and could have served as an abiotic phosphorus source for prebiotic chemistry. However, atomistic calculations of its degradation chemistry generally require quantum simulation approaches, which can be too computationally cumbersome to study sufficient time and length scales for this process. In this regard, we have created a computationally efficient semi-empirical quantum Density Functional Tight Binding (DFTB) model for iron and phosphorus-containing materials by adopting an existing semi-automated workflow that represents many-body interactions by linear combinations of Chebyshev polynomials. We have utilized a relatively small training set to optimize a DFTB model that is accurate for schreibersite physical and chemical properties, including its bulk properties, surface energies, and water absorption. We then show that our model shows strong transferability to several iron phosphide solids as well as multiple allotropes of iron metal. Our resulting DFTB parameterization will allow us to interrogate schreibersite aqueous decomposition at longer time and length scales than standard quantum approaches, providing for more detailed investigations of its role in prebiotic chemistry on early Earth.

Introduction

Phosphorous plays a central role in the formation of many life-building compounds, including nucleotides, phospholipids, adenosine triphosphate (ATP) for metabolic energy storage, and calcium phosphate (apatite) found in bone.^{1–5} Extraterrestrial sources such as meteoritic impacts could have served as one possible source of prebiotic phosphorous on early Earth,⁴ including those with the mineral schreibersite, $(\text{Fe},\text{Ni})_3\text{P}$.^{6,7} Schreibersite is a ferromagnetic material with tetrahedral symmetry (orthogonal lattice constants with $a = b > c$). It has been suggested to play a role in the formation of prebiotic organics,^{4,6,8,9} where experimental studies have shown that it can catalyze the formation of amino acids, sugars,

and nucleotides.^{1,9,10} However, early Earth likely experienced a wide range of conditions, including electrical storms¹¹ and extreme thermodynamic conditions due to impacts,^{12–14} that are difficult to probe with experimental trial and error alone. Schreibersite degradation studies would thus benefit from atomistic simulations, which can identify specific reaction mechanisms and kinetics, and can help narrow the relevant thermodynamic conditions for prebiotic synthesis.

To date, computational studies on schreibersite have largely focused on quantum simulations of bulk properties and water surface adsorption using Kohn-Sham Density Functional Theory (DFT).^{15–17} DFT is known to yield accurate descriptions of condensed phase physical and chemical data, as well as the energetics of chemical bond breaking and forming under reactive conditions (e.g., Refs. 12,14). However, DFT simulations generally require heavy computational effort, which limits calculations to systems containing few hundreds of atoms and to molecular dynamics (MD) timescales of tens of picoseconds. These scales are generally orders of magnitude smaller than those probed by experiments, where for example, chemistry at elevated pressure and temperature can require nanoseconds or longer to equilibrate,^{18,19} and extended structures can form that are nanometer-scale in diameter.^{20,21} Reactive MD models can help alleviate this time and length scale gap by optimizing empirical²² or machine-learning functional forms^{23–26} to DFT or other quantum mechanical data. These methods are generally fit to the properties of specific chemical reactants over a narrow range of thermodynamic conditions. As a result, they can yield high computational efficiency, but tend to yield completely unphysical results outside of their fitting regime.

The Density Functional Tight Binding method (DFTB) represents a promising alternative for simulations of reactive materials. DFTB is an approximate quantum simulation technique whereby the majority of the electronic interactions are represented by a minimal atomic basis set and are precomputed and mapped to a radial grid.^{27–29} The DFTB total energy expression contains an empirical repulsive energy E_{rep} that can be fit to experimental or high-level computational data in order to extend the technique to a wide variety of mate-

rials and conditions.³⁰ There is considerable flexibility in the E_{Rep} functional form, including cubic splines,³¹ Gaussian Process Regression,³² many-body polynomial based representations,³³ and neural network potentials.³⁴ The DFTB methodology allows for several orders of magnitude increase in computational efficiency while retaining most of the accuracy of standard DFT simulations. Consequently, DFTB simulations can achieve close to chemical equilibrium timescales for reactivity under extreme conditions (~ 1 ns) using relatively low computational effort. One of the main limitations of DFTB, though, is the availability of existing repulsive energies in literature, as one repository of interaction parameters^{27,28,35–44} does not contain specific interactions between iron and phosphorus. In addition, the DFTB method itself has several hyperparameters, mainly the wavefunction and density confining radii (discussed below), that require challenging optimizations as well.

In this work, we overcome these issues for Fe_3P schreibersite by determining the Fe-Fe and Fe-P DFTB interaction potentials through a semi-automated workflow that uses the Chebyshev Interaction Model for Efficient Simulation (ChIMES) method for determination of the repulsive energies.^{45–47} ChIMES is a many-body reactive force field model for MD simulation based on linear combinations of Chebyshev polynomials. This linear parameterization yields rapid MD or E_{rep} model optimization, allowing us to efficiently cycle through large numbers of DFTB and ChIMES hyperparameters. DFTB/ChIMES models have been created for a wide variety of systems, including TiH_2 ,⁴⁸ energetic materials,¹⁹ actinides,⁴⁹ and as a general purpose model for organic materials.⁵⁰ Here, we first briefly review the DFTB and ChIMES approaches and explain our workflow for optimization of both DFTB and ChIMES hyperparameters. We then downselect our model through validation against a wide range of DFT data that was not included in our training set, such as the Fe_3P lattice constants, bulk moduli, surface facet energies, and bulk water absorption. We then examine our optimal DFTB/ChIMES model further by computing water surface adsorption energies, the phonon density of states of the perfect crystal, and MD simulations under ambient and extreme conditions. Finally, we explore the transferability of our model through the predic-

tion of properties for different materials, including FeP, Fe₂P, and three allotropes of iron. Our results indicate that our DFTB/ChIMES model yields comparable accuracy to DFT for all properties investigated here, including the intense pressures and temperatures that can be accessed during planetary impact.

Methods

DFT Calculations and Training Set Construction

All DFT simulations were performed using the Vienna Ab initio Simulation Package (VASP),^{51–53} with projector augmented wave (PAW) pseudopotentials^{54,55} and the Perdew, Burke, and Ernzerhof (PBE) exchange-correlation functional.⁵⁶ Partial occupancies of the electronic states were set with fourth-order Methfessel-Paxton smearing,⁵⁷ using a width of 0.2 eV. We observed converged energies for the bulk system with a plane-wave energy cut-off of 500 eV, self-consistent field (SCF) convergence criteria of 10^{-6} eV, and $6 \times 6 \times 6$ \mathbf{k} -point Monkhorst-Pack mesh sampling of Brillouin zone.⁵⁸ The force convergence tolerance for geometry optimizations was set to 0.01 eV/Å for each atom in each direction. Our calculations were performed with collinear spin polarization initialized in a ferromagnetic configuration, which was maintained during all optimizations. As mentioned in Ref. 15, the inclusion of van der Waals (vdW) correction in our calculations resulted in a constant offset of the water absorption energies, with minimal change to optimized configurations. Furthermore, the observed effect is strongly dependent upon the choice of the vdW functional.⁵⁹ Hence, for the model development in this study, we have chosen to adopt the standard PBE functional without vdW, though we note that those effects can be included at a later date.

Our training set was built by performing DFT-MD simulations of a 32 atom Fe₃P schreibersite supercell, initially optimized to dimensions of 9.045Å \times 9.045Å \times 4.380Å, yielding a density of 7.36 g/cm³. We then used the relaxed structure to initiate 20 ps long DFT-MD trajectories with a timestep of 1.0 fs at temperatures of 300, 1500, and 2000 K

and pressures of 0, 10, 20, 30, and 40 GPa. From these simulations, we then aggregated the following 310 training configurations in total:

- 120 configurations equally spaced in time (e.g., sampled every \sim 167 fs from the MD trajectory) at $P = 0$ GPa and $T = 300, 1500$, and 2000 K.
- 120 equally spaced configurations at $P = 10, 20, 30$, and 40 GPa and $T = 1500$ K.
- 70 configurations obtained by randomly displacing by 0.1 Å the atoms of the optimized Fe_3P structure, similar to previous reactive MD model development.²⁶

DFTB calculations

DFTB calculations were performed with the DFTB+ code²⁹ using orbital resolved self-consistent charge calculations (SCC)⁶⁰ with a convergence criteria of 2.72×10^{-5} eV (10^{-6} au). We adopted the same electron thermal smearing and \mathbf{k} -point mesh of our DFT calculations. Similarly, all DFTB calculations were performed with collinear spin polarization initialized in a ferromagnetic spin geometry. The DFTB formalism has been extensively discussed in literature,^{27–29,61,62} with a brief outline provided here. The total energy expression with SCC is derived by assuming spherically symmetric charge densities and then expanding the Kohn-Sham total DFT total energy expression to either second²⁷ or third order⁶³ about small charge fluctuations. We note that in this work we rely on the second-order charge fluctuation model only.

The resulting total energy expression reads as:

$$E_{\text{DFTB}} = E_{\text{BS}} + E_{\text{Coul}} + E_{\text{rep}}. \quad (1)$$

Here, E_{BS} is the band structure energy, which is computed from the Kohn-Sham eigenstates determined from diagonalization of the approximate Hamiltonian with a minimal, Slater-type basis set. The term E_{Coul} corresponds to the charge-transfer energy from second-order

charge fluctuations and is computed self-consistently. Finally, E_{rep} is the repulsive energy, which contains the ion-ion repulsions, as well as Hartree and exchange-correlation double counting terms. E_{rep} is generally represented as a short-ranged empirical function that includes first coordination shell or bonded interactions only. Its parameters are usually fit to reproduce DFT or experimental data, and it can describe pairwise^{30,64} or many-body interactions.^{19,33,49,50,65} The Hamiltonian and overlap matrices used in E_{BS} are determined from pretabulated Slater-Koster (SK) tables that assume two-center interactions, only. However, prior to SK tabulation, both the electronic wave functions and electron density are subjected to separate confining or compression potentials, which has the effect of improving transferability of the calculations. For our work, we use the following simple power function for confinement:

$$V_{\text{conf}}(r) = \left(\frac{r}{R_{\chi}} \right)^2, \quad (2)$$

where $\chi = \Psi$ or n , R_{Ψ} corresponds to wavefunction compression, and R_n to density compression. Previous efforts have used larger exponents in the power function or alternate functional forms (e.g., Ref. 66), which can be investigated in future work.

In general, optimal choice of confining radii is system-dependent and cannot be determined *a priori*, frequently requiring a semi-exhaustive search.^{33,67} In our study, we choose to focus on optimizing the Fe density and wavefunction confining radii, only, in order to make our search more tractable. Similarly, we have only created E_{Rep} models for Fe-Fe and Fe-P interactions. The remaining DFTB+ interaction potentials (including tabulated SK Hamiltonian and overlap matrices, and/or E_{Rep} functions) were taken from known parameter sets. All non-iron interactions, such as those involving P, O, and H were taken from the mio-1-1 parameter set.^{27,63} The Fe-O and Fe-H repulsive energies were determined by first computing new SK tables using our choice of confining radii for Fe and those from mio-1-1 for O and H. This was followed by matching energetics for dimer calculations from the trans3d parameter set⁴⁴ to approximate the repulsive energies. A recent publication has made available

DFTB parameterizations for a large portion of the periodic table,⁶⁸ though these were not available at the time of this study and have not been tested for schreibersite/water systems, specifically.

ChIMES Methodology and Many-body E_{Rep} determination

The ChIMES method has been discussed in detail elsewhere,^{45–47,67} and hence will only be given a short introduction here. The starting point in ChIMES is a many-body expansion of the total energy of the system:

$$E_{\text{DFT}} = \sum_{i_1}^{n_a} {}^1E_{i_1} + \sum_{i_1 > i_2}^{n_a} {}^2E_{i_1 i_2} + \sum_{i_1 > i_2 > i_3}^{n_a} {}^3E_{i_1 i_2 i_3} + \sum_{i_1 > i_2 > i_3 > i_4}^{n_a} {}^4E_{i_1 i_2 i_3 i_4} + \dots + \sum_{i_1 > i_2 \dots i_{n_B-1} > i_{n_B}}^{n_a} {}^{n_B}E_{i_1 i_2 \dots i_{n_B}}. \quad (3)$$

Here, the index n_a allows for a sum over the total number of atoms. The one-body contributions (${}^1E_{i_1}$) are element-specific constants, the two-body (2B) or dimer contributions (${}^2E_{i_1 i_2}$) correspond to pair-wise interactions, the three-body (3B) or trimer contributions (${}^3E_{i_1 i_2 i_3}$) to triplet energies, etc., until a user-defined maximum of n_B is reached.

We now express each of the greater than one-body terms as a sum of linear combinations of Chebyshev polynomials of the first kind. In this case, $T_m(x)$ corresponds to a Chebyshev polynomial of order m , and $x = \cos \theta$, which limits the Chebyshev polynomial range to $[-1 : 1]$. For the 2B energy ${}^2E_{i_1 i_2}$, we use the following expression:

$${}^2E_{i_1 i_2} = f_p(r_{i_1 i_2}) + f_c^{e_{i_1} e_{i_2}}(r_{i_1 i_2}) \sum_{m=1}^{N_{2B}} C_m^{e_{i_1} e_{i_2}} T_m(s_{i_1 i_2}^{e_{i_1} e_{i_2}}) \quad (4)$$

Starting with the terms in the summation, $C_m^{e_{i_1} e_{i_2}}$ is the permutationally invariant coefficient for m th order polynomial (taken to maximum order of N_{2B}) for pairwise interactions between atoms i and j , which are represented by element types e_{i_1} and e_{i_2} . The term $s_{i_1 i_2}^{e_{i_1} e_{i_2}}$ is the transformed pairwise distance ($r_{i_1 i_2}$) such that the user-defined radial range $[r_{\min}^{e_{i_1} e_{i_2}} : r_{\max}^{e_{i_1} e_{i_2}}]$ is scaled to $[-1 : 1]$, using an element-pair specific scaling function. Similar to previous

work,⁴⁵ we rely on the Morse-like exponential function, where $r_{i_1 i_2}$ is scaled by a user chosen constant $\lambda_{e_1 e_2}$, i.e., $s_{i_1 i_2}^{e_1 e_2} \propto \exp(-r_{i_1 i_2}/\lambda_{e_1 e_2})$. The value of $\lambda_{e_1 e_2}$ is usually taken to be the peak position of the first coordination shell from the radial distribution function for that element pair. We ensure smooth behavior and zero energy at the radial boundary ($r_{\max}^{e_1 e_2}$) through the term $f_c^{e_1 e_2}(r_{i_1 i_2})$, which we take to be is a Tersoff smoothing function.⁶⁹ Lastly, we use a smoothly varying penalty function $f_p(r_{i_1 i_2})$ in order to prevent sampling of distances below the minimum value sampled in our training set ($r_{\min}^{e_1 e_2}$), thus preventing calculation of the Chebyshev polynomials outside of their natural range.

Greater than two-body terms can be determined through creation of many-body orthogonal polynomials. These can be obtained by defining a cluster of size n and taking the tensorial product of the Chebyshev polynomials derived from the constituent $\binom{n}{2}$ unique pairs. In this case, the three-body polynomials will be products of $\binom{3}{2} = 3$ two-body polynomials, i.e.:

$${}^3E_{i_1 i_2 i_3} = f_c^{e_1 e_2}(r_{i_1 i_2}) f_c^{e_1 e_3}(r_{i_1 i_3}) f_c^{e_2 e_3}(r_{i_2 i_3}) \sum_{m=0}^{N_{3B}} \sum_{p=0}^{N_{3B}} \sum_{q=0}^{N_{3B}'} C_{mpq}^{e_1 e_2 e_3} T_m(s_{i_1 i_2}^{e_1 e_2}) T_p(s_{i_1 i_3}^{e_1 e_3}) T_q(s_{i_2 i_3}^{e_2 e_3}) \quad (5)$$

The triple sum over the three-body polynomials is taken over the hypercube up to a predefined order N_{3B} , and the primed sum denotes that we include only terms for which two or more of the polynomial powers are greater than zero (to guarantee that three distinct triplets are evaluated). Four-body (4B) terms are similarly included in ChIMES optimizations,²⁶ where ${}^4E_{i_1 i_2 i_3 i_4}$ is now determined from the sum over the product of the $\binom{4}{2} = 6$ constituent pair-wise polynomials multiplied by a single permutationally invariant coefficient.

The training set for the E_{Rep} was then created by computing the DFTB quantum mechanical terms for each configuration (e.g., E_{BS} and E_{Coul}) and subtracting these quantities from the corresponding DFT data. This generally includes the cartesian forces, \vec{F} , stress tensor components, $\bar{\sigma}$, and the total system energy. Optimal ChIMES parameters (the coefficients of linear combination) can then readily be determined through linear least squares fitting of the overdetermined matrix equation $\mathbf{wAC} = \mathbf{wB}_{\text{rep}}$. The matrix \mathbf{A} corresponds to the

derivatives of the ChIMES energy or force expression with respect to the fitting coefficients (i.e., the unweighted polynomial values, including the smoothing function). The column vectors \mathbf{C} and \mathbf{B}_{rep} correspond to the linear ChIMES coefficients for which we are solving and the numerical values for the training data, respectively. The symbol \mathbf{w} corresponds to a diagonal matrix of weights to be applied to the elements of \mathbf{B}_{rep} and rows of \mathbf{A} .

The Chebyshev polynomial coefficients can then be solved for by minimizing the objective function:

$$F_{\text{obj}} = \sqrt{\frac{1}{N_d} \times \left(\sum_{\tau=1}^M \sum_{i=1}^{n_a} \sum_{\alpha=1}^3 w_{F_{\alpha_i}}^2 (\Delta F_{\alpha_i})^2 + \sum_{\tau=1}^M \sum_{\alpha=1}^3 w_{\sigma_{\alpha\alpha}}^2 (\Delta \sigma_{\alpha\alpha})^2 + \sum_{\tau=1}^M w_{E_{\tau}}^2 (\Delta E_{\tau})^2 \right)}. \quad (6)$$

Here, M is the total number of configurations in the training set, N_d is the total number of data entries ($3Mn_a$ force components plus $3M$ stress tensor components plus M energy components), the w values correspond to the weights, and $\Delta F_{\alpha_i} = F_{\text{ChIMES}_{\alpha_i}}^{\tau} - F_{\text{Rep}_{\alpha_i}}^{\tau*}$, $\Delta \sigma_{\alpha\beta} = \sigma_{\text{ChIMES}_{\alpha\beta}}^{\tau} - \sigma_{\text{Rep}_{\alpha\beta}}^{\tau*}$, and $\Delta E_i = E_{\text{ChIMES}}^{\tau} - E_{\text{Rep}}^{\tau*}$. In this case, $F_{\text{Rep}_{\alpha_i}}^{\tau*}$, $\sigma_{\text{Rep}_{\alpha\beta}}^{\tau*}$, and $E_{\text{Rep}}^{\tau*}$ correspond to the residuals determined from the difference between the DFT computed quantities and those computed from DFTB without the repulsive energy for i th atom in the τ th configuration, and α/β correspond to the Cartesian direction. Previous work has indicated that forces and the diagonal stress tensor components can be the most significant data for E_{Rep} determination.^{19,30,67} Consequently, for Fe₃P DFTB/ChIMES model development, we have chosen to optimize to these quantities, only.

We then optimized the DFTB+ confining radii and ChIMES hyperparameters through a workflow similar to our previous efforts⁶⁷ (Figure 1). For ChIMES E_{Rep} parametrization, we set the minimum and maximum element-pair radii to span the first coordination shell of the configurations in our training set: $1.6 \leq r_{\text{FeFe}} \leq 3.5 \text{ \AA}$ and $1.5 \leq r_{\text{FeP}} \leq 2.9 \text{ \AA}$. We use Morse-like scaling constants of $\lambda_{\text{FeFe}} = 2.6$ and $\lambda_{\text{FeP}} = 2.25$, which correspond to the average nearest neighbor distances in our training set. We have limited our search to the following sets of $\{n_{2\text{B}}, n_{3\text{B}}, n_{4\text{B}}\}$ ChIMES polynomials orders: $\{8, 4, 0\}$, $\{12, 8, 0\}$, $\{12, 8, 4\}$, and $\{16, 12, 0\}$. We have also applied different weights to stress tensor components, with

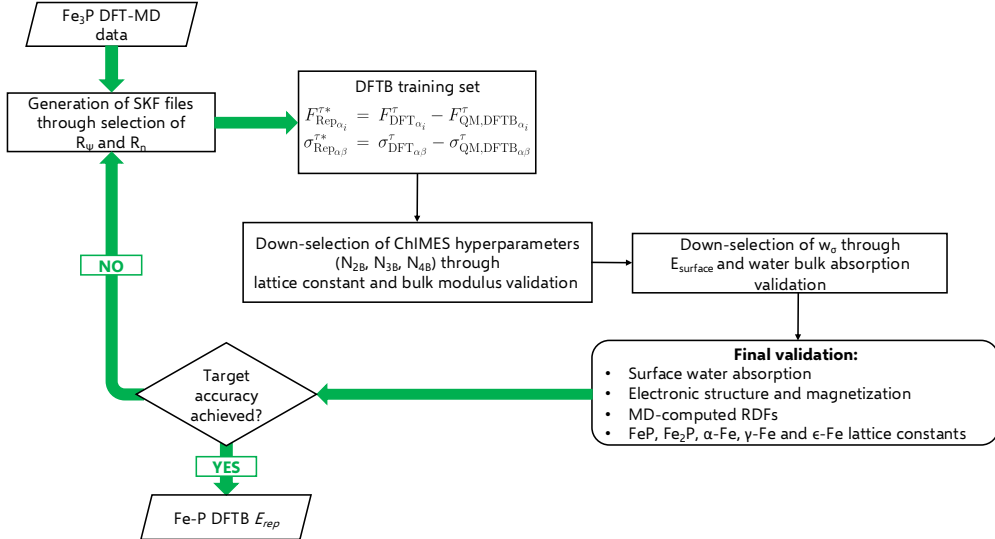


Figure 1: Workflow for DFTB/ChIMES optimization.

values of $w_\sigma = 1, 5, 10, 25, 50$, in order to improve agreement with the validation data.

Results and discussion

R_Ψ and R_n Optimization

We have computed a grid of DFTB Hamiltonian and overlap matrix SK tables that span values of $3.2 \leq R_\Psi \leq 5.0$ au and $6.0 \leq R_n \leq 17.0$ au, for a total of 30 different combinations of R_Ψ and R_n . These parameterizations were then passed through our workflow in order to create a unique ChIMES repulsive energy for each set of $\{R_\Psi, R_n\}$. We find that in general that smaller R_Ψ and R_n are associated with smaller force and stress root-mean-squared errors (RMSE). For example, the $\{8, 4, 0\}$ model set with $w_\sigma = 1$ yielded Fe force errors on the order of 8.1 kcal/mol.Å, P force errors 5.4 kcal/mol.Å, and stress tensor errors of 4.5 GPa for $\{R_\Psi = 3.2$ au, $R_n = 6.0$ au $\}$, in contrast to values of 16.6 kcal/mol.Å, 13.4 kcal/mol.Å, and 4.14 GPa for $\{R_\Psi = 5.0$ au, $R_n = 17.0$ au $\}$. The force RMSE exhibits relatively small changes with increasing stress tensor weight, though setting $w_\sigma = 50$ decreases the stress errors to < 1 GPa. Increasing the polynomial order of the ChIMES model has the overall

effect of lowering the RMSE. For example, the $\{16, 12, 0\}$ model set yields Fe force errors of approximately 7.8 kcal/mol.Å, P forces of 5.1 kcal/mol.Å, and stress tensor errors of 2.7 GPa for $\{R_\Psi = 3.2 \text{ au}, R_n = 6.0 \text{ au}\}$ and $w_\sigma = 1$. (Please see Supporting Information for additional data.).

The resulting DFTB/ChIMES models were then validated against a number of properties previously computed results from DFT calculations¹⁵ that were not a part of our training set. This includes the Fe_3P lattice constants, bulk modulus, surface energies for the (001), (100), and (110) crystal facets, and water bulk absorption and surface adsorption energies. All DFTB/ChIMES validation calculations were performed using the same k-point meshes as the DFT results, namely, bulk systems were run using a $6 \times 6 \times 6$ \mathbf{k} -point Monkhorst-Pack grid, while a $1 \times 7 \times 7$ mesh was used for the surface calculations, with a smaller mesh value in the surface direction. We again used orbital resolved SCC with a charge convergence criteria of 2.72×10^{-5} eV (10^{-6} au) and a force convergence tolerance of 0.01 eV/Å for each atom in each direction.

We now report on the results from our validation calculations. In general, we find that the inclusion of 4B terms in the $\{12, 8, 4\}$ parameterization yields only very change small in accuracy relative to the $\{12, 8, 0\}$ set. Hence, for the sake of brevity, we limit our discussion to the $\{8, 4, 0\}$ and $\{16, 12, 0\}$ parameterizations, which are the lowest and highest limits of ChIMES complexity in our study (the complete set of results can be found in the Supporting Information).

Lattice constants. Our results for the relative difference between the $\{8, 4, 0\}$ model and DFT for the schreibersite equilibrium lattice constants (Fig. 2 for the a constant, with results for c included in the Supporting Information) indicate that using equal weights in our optimizations for the forces and stress tensor components ($w_F = w_\sigma = 1$) consistently yields an overly compact lattice, where the values of a and c are approximately 8% and 10% smaller than those from DFT. These higher density structures also optimize to antiferromagnetic

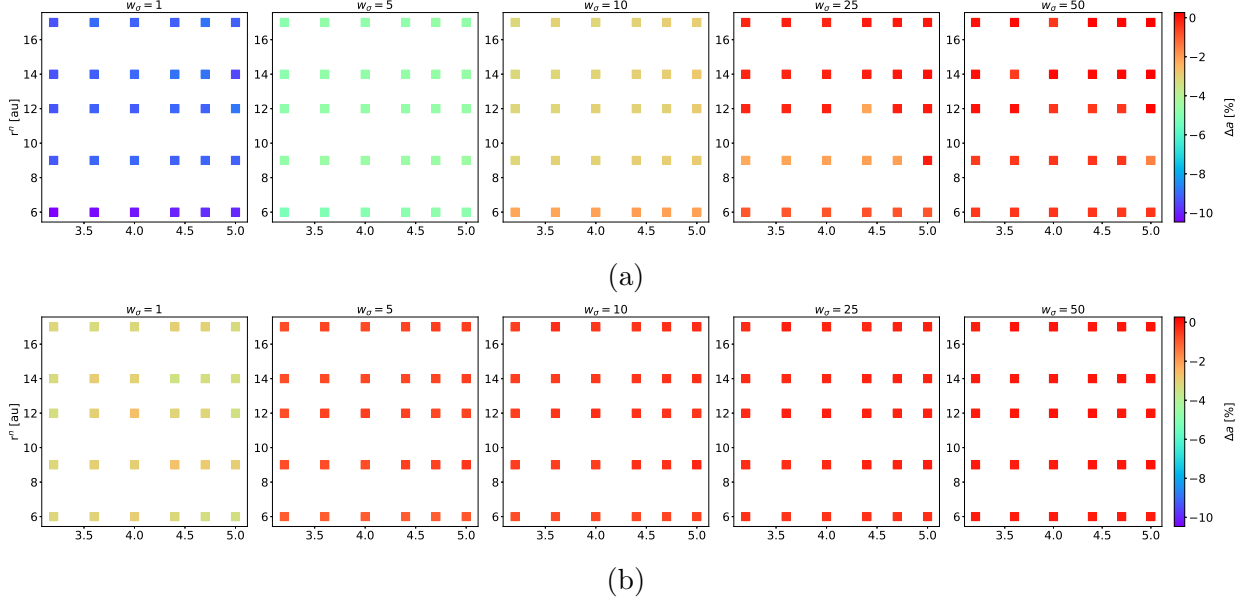


Figure 2: Percentage deviation from DFT values of the schreibersite a lattice constant for (a) $\{8,4,0\}$, and (b) $\{16,12,0\}$ model sets, as a function of the stress tensor weights (reported above the plots). Results for the c lattice constant are included in the Supporting Information.

spin geometries, rather than the correct ferromagnetic result. In addition, we observe a relatively small dependence on values of R_Ψ and R_n . However, the introduction of weights of $w_\sigma > 1$ while keeping w_F at unity improves the results appreciably, where observe the errors improve to -5% for $w_\sigma = 5$ to $\sim 1\%$ for $w_\sigma = 25, 50$.

Increasing the polynomial order to $\{16, 12, 0\}$ uniformly improves the lattice constant results relative to DFT. Here, the average error in a and c is $\sim 3.5\%$ for $w_\sigma = 1$, which decreases to $< 0.5\%$ for $w_\sigma = 25, 50$. We observe only small differences between results for $\{12, 8, 0\}$ and $\{12, 8, 4\}$, where the lattice constants both agree within 1% for values of $w_\sigma = 10$ and 25 (see Supporting Information for detailed data).

Bulk modulus. We now investigate the influence the confining radii on the schreibersite bulk modulus in order to test the validity of our models for high-pressure material property prediction. In this case, we have computed the zero temperature compression curves by isotropically compressing the system pressure to 100 GPa with each DFTB/ChIMES model.

We then determine the bulk modulus K_0 through optimization to a Rose-Vinet equation of state.⁷⁰ For reference, we previously obtained a DFT bulk modulus of $K_{\text{DFT}} = 173.2$ GPa,¹⁵ compared to two available experimental results of 172.0⁷¹ and 157.9⁷² GPa.

Fig. 3 reports the results in terms of relative difference ΔK_0 with respect to DFT. We find that all results for $w_\sigma = 1$ yield bulk moduli that are up to 400% too high for the $\{8, 4, 0\}$ set, and over 100% too high for the $\{16, 12, 0\}$ set. This is due to the excessively compact antiferromagnetic structure present in all of these DFTB/ChIMES models. We observe that applying values of w_σ greater than one yields improved results. The $\{8, 4, 0\}$ model set yields errors of approximately 100% for $w_\sigma = 5$, and errors approaching zero for $w_\sigma = 25$ and greater. Our results for $\{16, 12, 0\}$ initially converge more rapidly to low error results, where we observe a number of DFTB/ChIMES optimizations that yield errors of close to zero for $w_\sigma = 5$ and 10. However, the relative values of ΔK_0 increase with higher values of w_σ . This is likely because the large stress tensor weights combined with the higher complexity of the model yield higher errors in the forces overall. In general, we find that the $\{16, 12, 0\}$ model set generally yields the highest level of accuracy for our validation studies. Hence, we choose to focus on this model set for the remainder of our confining radii study.

Surface Energies. Next, we have investigated the surface formation energy for the (001), (100), and (110) low index surface facets. The surface formation energy is defined as

$$E_{\text{surface}} = \frac{E_{\text{slab}} - n \left(\frac{E_{\text{bulk}}}{n_{\text{bulk}}} \right)}{2A}. \quad (7)$$

Here, E_{slab} is the total electronic energy of the slab, $(E_{\text{bulk}}/n_{\text{bulk}})$ is the energy per atom of the bulk cell, n is the number of atoms contained in the slab, A is the surface area of a given facet, and the factor of two accounts for both surfaces present in a periodically replicated system. We use our previously computed surface structures from DFT as our initial configuration for the DFTB/ChIMES calculations. In this case, each surface slab is six atomic layers thick (corresponding to a total of 96 atoms) and with a vacuum region of

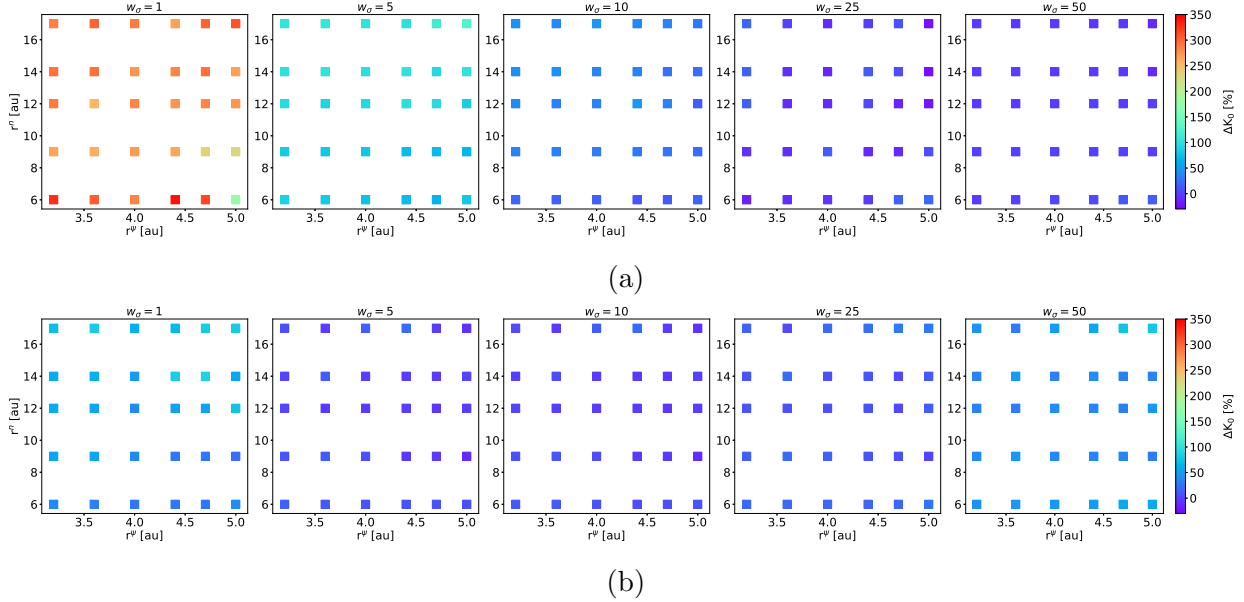


Figure 3: Percentage deviation from DFT bulk modulus of schreibersite for (a) the $\{8, 4, 0\}$ set and (b) $\{16, 12, 0\}$ set a function of stress tensor weights (reported above the plots).

20 Å in each direction perpendicular to the slab surface in order to minimize nonphysical interactions between periodic images. Furthermore, due to the heterogeneity of the system, each facet was constructed with different surface terminations (i.e., the number of P or Fe atoms at the surface). By enforcing both symmetry (top and bottom layers are identical) and stoichiometry (i.e., the system maintains a 3:1 iron to phosphorus ratio), we were able to build two different surface terminations for each facet, where either a majority of iron (labeled ‘type 1’) or phosphorus atoms (labeled ‘type 2’) is present. The errors for the (001) and (100) surfaces were similar for all sets of confining radii. Hence, for our discussion, we choose to focus on both types of the (001) and (110) surfaces, only.

The complete set of formation energies is reported in the Supporting Information. Our results for $\{16, 12, 0\}$ show that the energies for both type 1 and type 2 (001) surfaces are highly sensitive to the value of w_σ (Fig. 4). When no weights are applied the stress tensor components, the surface energy can be up to 60% larger than DFT (first panel on the left of Fig. 4a), with the highest value of $E_{001}^{(1)} = 3.66 \text{ J/m}^2$ from $R_\Psi = 3.2 \text{ au}$ and $R_n = 12 \text{ au}$ compression radii for the type 1 iron dominated surface, compared to the DFT value of 2.24

J/m^2 . We find that increasing the w_σ to 5 or 10 improves the results significantly, where surface energies with $R_\Psi > 4.4$ au deviate from DFT for both type 1 and 2 surfaces by less than 5%, with values of $E_{001}^{(1)}$ of 2.15 and 2.33 J/m^2 , each. Increasing w_σ to even larger values yields significantly larger errors, where the $w_\sigma = 25$ set yields surface energies that are 20-30% higher for $R_\Psi \leq 4.4$ au, with values of $E_{001}^{(1)}$ between 2.67 and 3.02 J/m^2 . This is again likely due to large errors in the forces for this set, which results in large errors in optimized geometries.

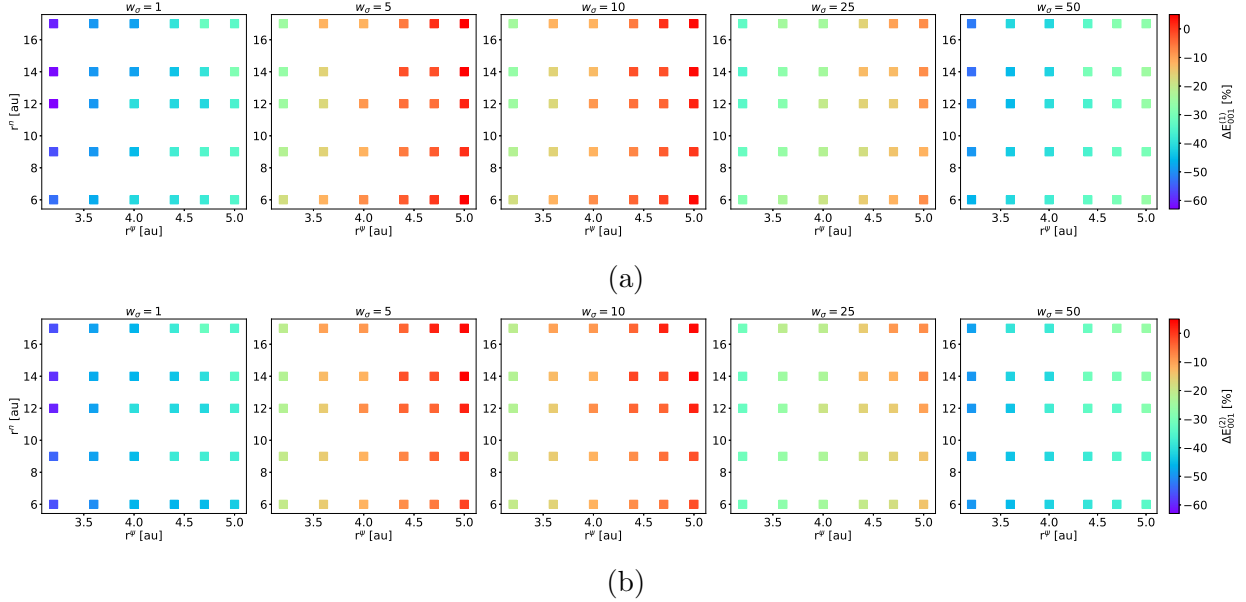


Figure 4: Percentage deviation from DFT values of schreibersite surface energy formation for (001) facets of termination type 1 (a) and type 2 (b) obtained for $\{16, 12, 0\}$.

In contrast, the effect of different confining radii on the (110) surface energy was a bit more difficult to characterize (Fig. 5), as our set of DFTB/ChIMES models for the $\{16, 12, 0\}$ set were more likely to be overfit. This resulted in a lack of convergence of a number of our surface optimizations, as indicated by the lack of data points for some combinations of $\{R_\Psi, R_n\}$. However, we still observe a similar trend for both type 1 and type 2 surfaces, where values of $R_\Psi > 4.0$ and $w_\sigma = 5$ or 10 yielded the smallest deviations from DFT. For example, the DFTB/ChIMES model obtained with $\{R_\Psi = 4.7$ au, $R_n = 9.0$ au $\}$ and $w_\sigma = 10$ yielded an error of $\sim 3\%$ for the type 1 surface and 22% of the type 2 surface, with

values 2.61 and 1.88 J/m², compared to the DFT results of 2.53 and 1.54 J/m², respectively. It is likely the difficulties with convergence for this set would be improved with additional training data, which is the subject of future work.

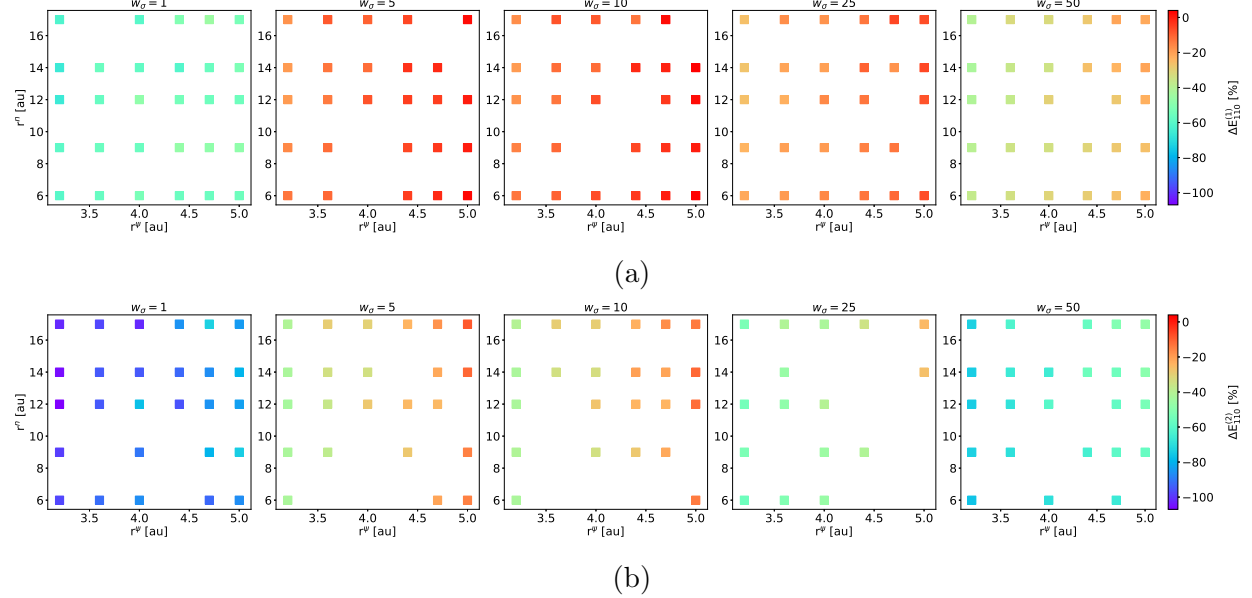


Figure 5: Percentage deviation from DFT values of schreibersite surface energy formation for (110) facets of termination type 1 (a) and type 2 (b) obtained for {16, 12, 0} as a function of stress weights.

Bulk interstitial water absorption. We now examine the interaction of schreibersite with water molecules in the bulk. We have used the PyMatGen code⁷³ to identify two distinct interstitial sites within the lattice (Fig. 6). Specifically, the first type of interstitial site (site 1) consists of a tetrahedral cage composed of iron atoms. The second type of interstitial site (site 2) is formed by a tetrahedron that incorporates a phosphorus atom at one of its vertices. The formation energies for these sites are calculated via the equation $E_{\text{def}} = E_{\text{Fe}_3\text{P+H}_2\text{O}} - (E_{\text{bulk}} + E_{\text{H}_2\text{O}})$, where $E_{\text{Fe}_3\text{P+H}_2\text{O}}$ represents the total energy of the relaxed defected structure, E_{bulk} is the total energy of the bulk schreibersite, and $E_{\text{H}_2\text{O}}$ denotes the energy of an isolated water molecule in vacuum. In this case, both DFT and all DFTB/ChIMES calculations were initiated from the same initial configurations, which resulted in dissociation of the water molecule upon optimization. For reference, the values

computed via DFT are $E_{\text{site1}} = -3.56$ eV and $E_{\text{site2}} = -3.49$ eV, respectively.

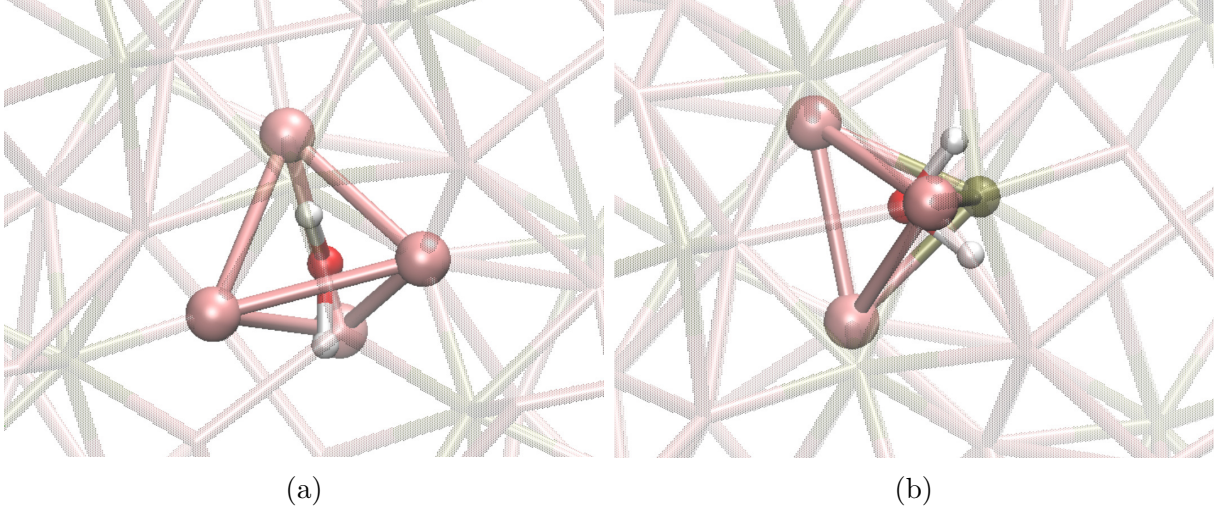


Figure 6: (Bulk interstitial sites for water absorption in schreibersite for (a) site 1 with only Fe atoms, (b) site 2 with one P atom as a vertex of the tetrahedral cage.

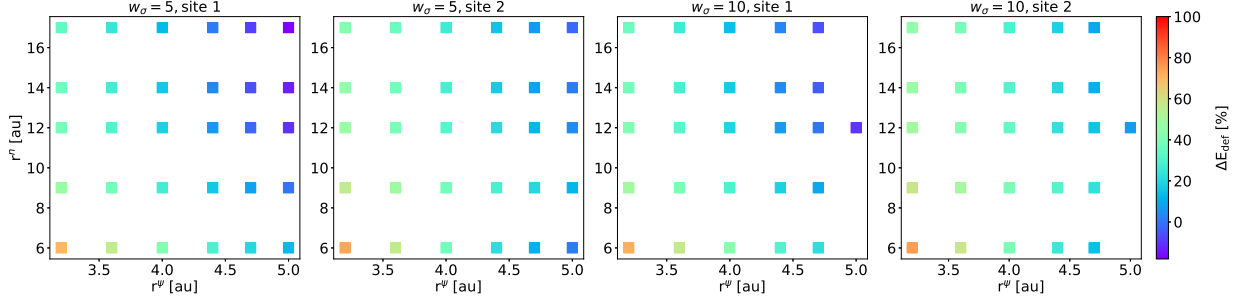


Figure 7: Percentage deviation from DFT values of schreibersite bulk water absorption for $\{16, 12, 0\}$ obtained for both interstitial sites and for $w = 5$ and $w = 10$.

Our sweep tests of confining radii for the $\{16, 12, 0\}/w_\sigma = 5, 10$ model sets indicate that in general these dissociative absorption energies are more accurately computed when considering longer confining radii (Fig. 7). For example, errors relative to DFT are minimized for the $w_\sigma = 5$ set when $R_\Psi = 5.0$ au and $R_n = 17.0$ au, with values of -3.49 and -3.88 eV, respectively for site 1 and site 2. However, we observe that smaller confining radii such as $R_\Psi = 4.7$ au and $R_n = 9.0$ au yield relatively small errors as well, with values of -3.64 and -3.22 eV for site 1 and site 2, respectively, when $w_\sigma = 5$. It is worth noting that, although the $w_\sigma = 10$ in general also exhibits high accuracy, it tends to be overfit when $R_\Psi = 5.0$

(indicated by the missing points in Fig. 7). The increased error with higher stress tensor weighting is commensurate with the higher error in predicted forces, discussed above. The errors are also generally highest for the $\{R_\Psi = 3.2 \text{ au}, R_n = 6.0 \text{ au}\}$ models due to over compression of the wavefunction and density.

Optimal Hyperparameters. Our findings thus far provide a broad picture of how the ChIMES hyperparameters and DFTB configuration influence the accuracy of our model. Given our results, we have chosen $\{R_\Psi = 4.7 \text{ au}, R_n = 9.0 \text{ au}\}$, $\{n_{2B} = 16, n_{3B} = 12, n_{4B} = 0\}$ as our optimal set of DFTB/ChIMES hyperparameters, with $w_\sigma = 5$ for the weights assigned to the stress tensor components (final results shown in Table 1). This model yielded the highest overall degree of accuracy while avoiding overfitting for our validation calculations. This model is able to predict the correct energetic ordering of absorption sites ($E_{\text{site}2} > E_{\text{site}1}$) with a somewhat large ΔE of 0.41 eV relative to our DFT calculations, though that value likely changes with the choice of functional and basis set.

Table 1

		DFTB/ ChIMES	DFT
Lattice constant [Å]	a	9.008	9.045
	c	4.366	4.380
K_0 [GPa]		170.3	173.2
(001) [J/m ²]	type 1	2.32	2.24
	type 2	2.10	2.00
(100) [J/m ²]	type 1	2.20	2.05
	type 2	2.05	1.95
(110) [J/m ²]	type 1	2.61	2.53
	type 2	1.88	1.54
E_{def} [eV]	Site 1	-3.64	-3.78
	Site 2	-3.22	-3.49

Water Surface Absorption Energies

We now test our optimal DFTB/ChIMES model for water absorption on the most stable facet, i.e., the (110) type 2 (phosphorus terminated) surface. Similarly to interstitial defects, we defined the adsorption energies as $E_{\text{ads}} = E_{\text{slab+H}_2\text{O}} - (E_{\text{slab}} + E_{\text{H}_2\text{O}})$ where $E_{\text{slab+H}_2\text{O}}$ is the energy of the Fe_3P slab with the adsorbed molecule in its final state, E_{slab} is the energy of the pristine slab, and again $E_{\text{H}_2\text{O}}$ is the energy of an isolated water molecule in vacuum. In our previous work,¹⁵ we identified three different adsorption sites, i.e., ‘ontop’, ‘bridge’ and ‘hollow’ (Fig. 8). Each type of site can involve different combinations of Fe or P atoms, resulting in two different site types for each classification. We thus validate our model against results for ontop sites on an iron or on a phosphorous atom, bridge sites between two iron atoms or one iron and one phosphorous, and two different hollow sites, with or without phosphorus, depending on the packing of the surface atoms. In addition, the computed adsorption energies for each site depend on the initial orientation of the water molecule, i.e., whether one of the hydrogen atoms from the water molecule is pointing up (‘*u*’) into the vacuum, down into the slab (‘*d*’), or the H_2O molecular plane is parallel to the schreibersite surface (‘*p*’).^{15,17} Hence, each adsorption site is examined for its *u*, *p*, and *d* dependence as well, for a total of 18 adsorption energies (Table 2).

We observe that the strength of the adsorption energies involving iron atoms are generally overestimated by DFTB/ChIMES relative to DFT, yielding values that are $\sim 0.22\text{-}0.25$ eV too negative for the Fe-Fe bridge site, $\sim 0.38\text{-}0.40$ eV too negative for the Fe-Fe-P hollow site, and $0.43\text{-}0.57$ eV too negative for the Fe ontop site. One exception is the Fe-Fe-Fe *p* hollow site, where our model agrees with DFT within 0.07 eV.

In contrast, the adsorption energies from DFTB/ChIMES predominantly involving phosphorus atoms tend to be more accurate, where the Fe-P bridge site results differ from DFT by less than 0.05 eV and the P ontop site by less than 0.04 eV. These discrepancies in the Fe results are likely due in part to the fact that the Fe-O and Fe-H pairwise repulsive energies were determined by matching to the trans3d parameter set, which were optimized for

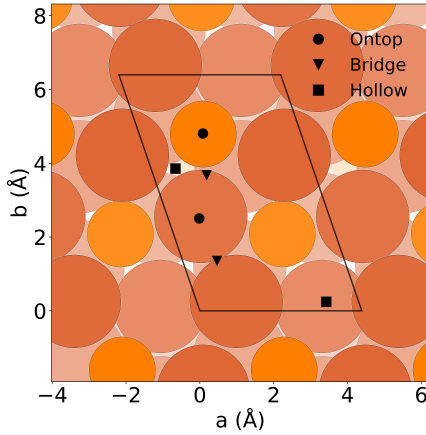


Figure 8: Different adsorption sites on (110) surface. In this image, the big brown circles represent iron atoms, while the smaller orange circles stand for the phosphorous atoms. Reproduced from Ref. 15. Copyright 2022 American Chemical Society.

Table 2: Adsorption energies for the different sites shown in Fig. 8, and for the initial molecular configurations investigated here. We note that ‘p’ stands for planar, ‘u’ stands for upward and ‘d’ for downward. Values for u, p , and d that are nearly isoenergetic indicate optimization to a similar final water molecule geometry.

		DFTB/ ChIMES	DFT
Bridge	Fe - Fe	(p) -0.649	-0.429
		(u) -0.694	-0.444
		(d) -0.693	-0.445
Hollow	Fe - P	(p) -0.152	-0.211
		(u) -0.156	-0.168
		(d) -0.156	-0.184
Hollow	Fe - Fe - P	(p) -0.710	-0.331
		(u) -0.710	-0.338
		(d) -0.728	-0.334
Ontop	Fe - Fe - Fe	(p) -0.188	-0.195
		(u) -0.729	-0.484
		(d) -0.725	-0.484
Ontop	Fe	(p) -0.799	-0.227
		(u) -0.720	-0.269
		(d) -0.702	-0.268
P	(p)	-0.145	-0.173
	(u)	-0.131	-0.162
	(d)	-0.125	-0.164

molecular data, whereas inclusion of periodic solids as well as chemical surface interactions can require additional optimizations.⁶⁷ However, the mio-1-1 parameters used for O, H, and P interactions were optimized to a properties of a relatively large series different molecules, yielding improved surface-molecule interactions.

Magentization as a Function of Pressure

Given one of our objectives of developing a model suitable for high-pressure impact studies, we consider the variation of magnetization in response to external pressure. Here, we have computed the relative magnetization in scheibersite as it is compressed at zero Kelvin from zero to 100 GPa (Fig. 9). Results from DFTB/ChIMES and DFT are very similar throughout the entire pressure range, with a gradual decrease up to 30 GPa, where we observe a rapid drop that corresponds to a potential first-order phase transition.^{71,72,74} This diminishing trend culminates in a non-magnetic state at $P > 50$ GPa in both DFT and DFTB/ChIMES, where the iron atoms have largely lost their magnetic moments, as previously noted by high-pressure experiments.⁷⁴

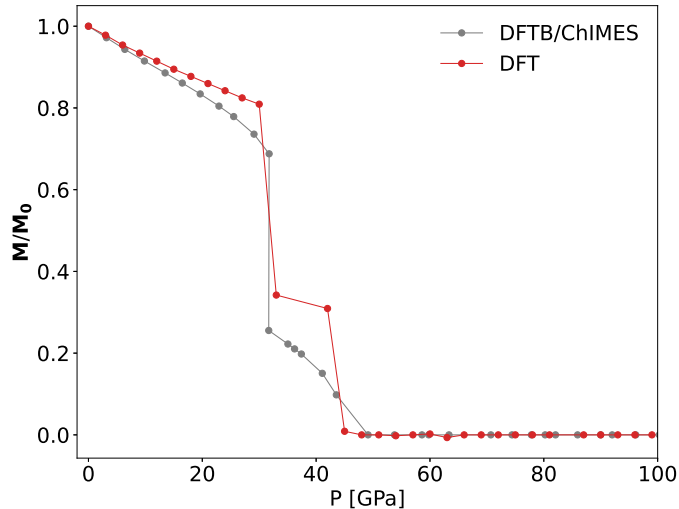


Figure 9: Normalized magnetization of Fe_3P as a function of external pressure.

Phonon Density of States

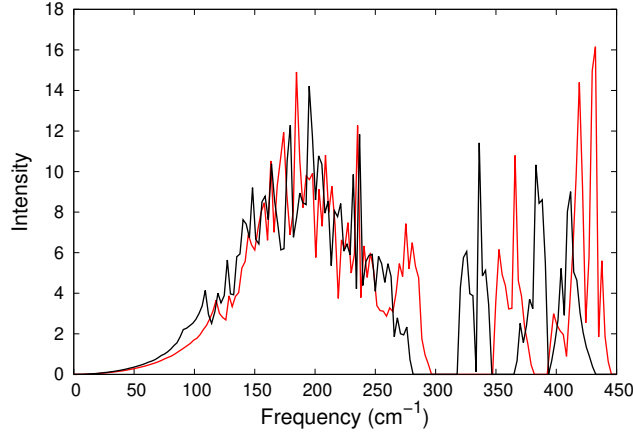


Figure 10: Phonon density of states, with results from DFTB/ChIMES in red and those from DFT in black.

We now examine the accuracy of the vibrational frequency from DFTB/ChIMES by computing the total phonon density of states (Fig. 10). These were computed from a zero-temperature optimized primitive cell with the phonopy code,^{75,76} using a $2 \times 2 \times 2$ supercell and a $31 \times 31 \times 31$ q-point (wavevector) mesh. Overall, we observe reasonable agreement between DFTB/ChIMES and DFT. The manifold of vibrational states between zero and ~ 300 cm^{-1} shows close agreement up to 250 cm^{-1} , though DFTB/ChIMES shows an enhanced density of states between 250 - 300 cm^{-1} that is not present in the DFT results. Both DFT and DFTB/ChIMES exhibit a doublet above 300 cm^{-1} , though the DFTB/ChIMES result occurs ~ 50 cm^{-1} higher. The remaining manifold of peaks from DFT occurs roughly between 360 - 430 cm^{-1} , and is somewhat different in shape compared to the DFTB/ChIMES result, which spans approximately 390 - 445 cm^{-1} . These deviations are relatively in magnitude, given that a difference of 50 cm^{-1} , for example, corresponds to a change in energy of $\sim 6 \times 10^{-4}$ eV.

Molecular Dynamics

In order to test the dynamics of our model under ambient and extreme conditions, we have performed molecular dynamics (MD) calculations using DFTB/ChIMES at pressures and temperatures from ambient up to 50 GPa and 1500 K. Both DFTB/ChIMES and DFT *NVT* simulations were initiated using an optimized 32-atom schreibersite bulk simulation cell, run for 5 ps and using a timestep of 1 fs. Here, we have used a $2 \times 2 \times 2$ \mathbf{k} -point Monkhorst-Pack grid for both sets of simulations.

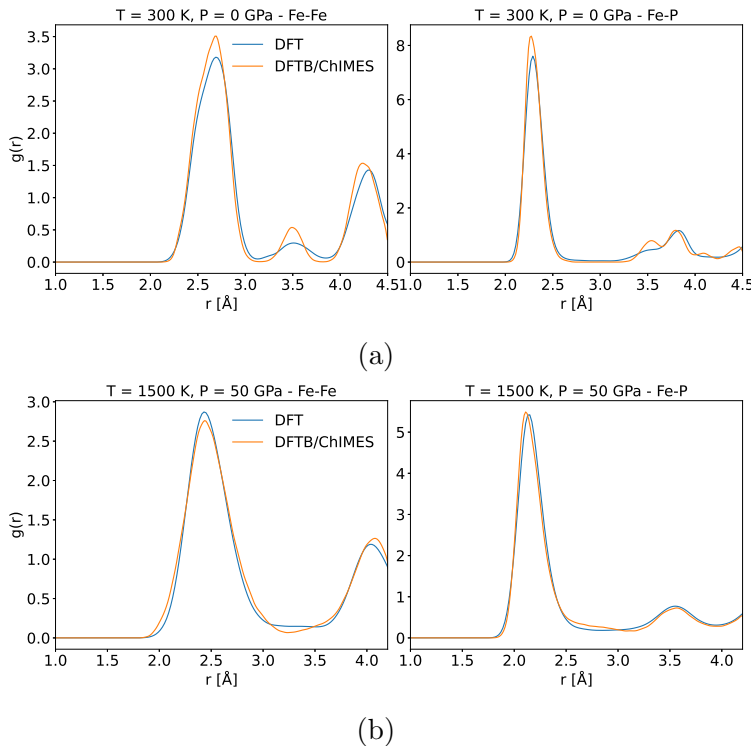


Figure 11: Radial distribution functions obtained for Fe-Fe and Fe-P interatomic distances in schreibersite, as a function of temperature and pressure. The top row (a) shows results for $T = 300\text{K}$ and $P = 0\text{ GPa}$, while the bottom row (b) corresponds to $T = 1500\text{K}$ and $P = 50\text{ GPa}$.

Our results for the Fe-Fe and Fe-P RDFs indicate overall very good agreement between the DFTB/ChIMES and DFT datasets (Fig. 11), where we have excluded the P-P RDFs for the sake of brevity. Simulations under ambient conditions (Fig. 11a) indicate that DFTB/ChIMES can effectively capture the first coordination shells, where we observe a

close match with DFT for the first peak in both the Fe-Fe and Fe-P RDFs. DFTB/ChIMES reveals a slightly less structured atomic distribution for the second and third coordination shells, though the differences are relatively small. At elevated temperatures and pressures (Fig. 11b), we observe strong agreement with DFT for all solvation shells captured within our simulations. Notably, configurations at $P = 50$ GPa were absent from our dataset, indicative of the ability of our model to accurately model state points beyond our training regime.

Transferability of the model

Finally, we examine the transferability of our DFTB/ChIMES model through lattice optimizations of materials other than Fe_3P schreibersite. All optimizations were performed using the material unit cells and the DFTB+ convergence criteria discussed above. We first performed calculations on two other iron phosphide structures, FeP and Fe_2P . Iron monophosphide (FeP) belongs to a family of transition-metal monopnictides, crystallizing in the MnP structure type (orthorhombic, space group Pnma). Recently, FeP has garnered attention due to its distinctive magnetic and superconducting properties, including the formation of a helical magnetic structure.⁷⁷ Di-iron phosphide (Fe_2P), has been investigated as an anode material in sodium-ion batteries.⁷⁸ Fe_2P crystallizes in a hexagonal crystal structure that can be described as layers of Fe atoms in a hexagonal close-packed arrangement with P atoms occupying half of the octahedral interstices.

Table 3: Comparison between DFTB/ChIMES, DFT, and experiments for the FeP and Fe_2P lattice constants.

	FeP			Fe_2P		
	DFTB/ ChIMES	DFT	expt ⁷⁷	DFTB/ ChIMES	DFT	expt ⁷⁹
a [\AA]	3.340	3.034	3.089		5.828	5.802
b [\AA]	5.356	5.133	5.174		5.876	
c [\AA]	5.745	5.694	5.772	3.340	3.408	3.449

Our optimization results for these two iron phosphides are summarized in Table 3. The

b and c lattice constants for FeP compare very well with DFT and experiment, with errors of $\sim 1\%$ and 4% , respectively. The a lattice constant differs by roughly 10% , though DFTB/ChIMES is able to retain the orthorhombic primitive cell. The Fe_2P optimization yields a somewhat closer comparison with DFT and experiment overall, where both a and c lattice constants agree within $\sim 1\text{-}2\%$.

We have also performed transferability studies on three allotropic forms of iron metal, including α -Fe, γ -Fe, and ϵ -Fe. Ferrite, or α -iron, is the ground state and corresponds to a ferromagnetic body-centered cubic (bcc) structure that remains stable up to 1185 K. Beyond this temperature but at low pressure, α -Fe transitions to the face-centered cubic (fcc) γ -Fe structure, also named austenite. Under pressures exceeding approximately 10-13 GPa and temperatures up to around 700 K, α -Fe adopts the hexagonal close-packed (hcp) ϵ -iron structure, also called hexaferrum.⁸⁰ The results of our calculations indicate strong agreement for the lattice constants of all three phases, with agreement of $\lesssim 1\%$ for both α -Fe and γ -Fe. The agreement for ϵ -Fe is also reasonable, where DFTB/ChIMES differs by $\sim 1\%$ or the a lattice constant, and by $\sim 4\%$ for the c lattice constant (Table 4). However, we observe some disagreement with DFT for the energetic ordering of the allotropes. In this case, DFT yields an energetic ordering of α -Fe followed by ϵ -Fe and γ -Fe, whereas DFTB/ChIMES yields ϵ -Fe as the most stable phase. However, ϵ -Fe is nearly isoenergetic with α -Fe for both sets of calculations, and the energetic difference between α -Fe and γ -Fe is similar, with a value of 0.13 eV from DFTB/ChIMES and 0.09 eV from DFT. Regardless, our results indicate the relatively strong transferability of DFTB/ChIMES to Fe/P-containing materials, given that none of these materials were present in our training set.

Conclusions

In this work, we have determined an optimal DFTB/ChIMES model in order to conduct quantum simulations of chemical reactivity due to the meteoritic mineral schreibersite. We

Table 4: Comparison of the DFTB/ChIMES with DFT and experimental values of the different iron allotropes’ lattice constants and energy per atom. In particular, the energetic ordering is given with respect to the most stable structures, which has a 0.0 eV value in the table.

	α -Fe			γ -Fe			ϵ -Fe		
	DFTB/ ChIMES	DFT	expt ⁸¹	DFTB/ ChIMES	DFT	expt ⁸²	DFTB/ ChIMES	DFT	expt ⁸³
a [Å]	2.827	2.831	2.856	3.647	3.630	3.6519	2.464	2.484	2.461
c [Å]							3.715	3.898	3.952
ΔE [eV]	0.022	0.000		0.157	0.093		0.000	0.072	

have used our workflow to optimize the DFTB semi-empirical Hamiltonian and overlap matrices, while simultaneously determining a many-body ChIMES repulsive energy. The advantage to our workflow stems from the rapidity with which the linear ChIMES parameters can be determined for each set of quantum interactions, as well as the relatively small data requirements for our repulsive energy optimizations. Our DFTB/ChIMES workflow can be performed with a semi-automated approach, allowing for a rapid down selection of DFTB confining radii, which can be cumbersome to optimize, otherwise.

Our DFTB/ChIMES model yields accurate results for the validation of our study, indicative of a robust model for simulations of Fe_3P degradation due to planetary impact. This included a wide diversity of data, such as the scherbersite lattice constant, bulk modulus, and low-index surface energies. We also compute relatively accurate results for bulk water absorption and water surface adsorption, though these results could be improved further by including these types of systems in our optimization workflow. Regardless, DFTB/ChIMES can determine a highly accurate representation of the magnetization as a function of increasing pressure, where results compare closely with DFT in terms of a schreibersite phase transition at approximately 30 GPa and the absence of magnetization above 50 GPa. Furthermore, our model is shown to be robust for molecular dynamics simulations under extreme pressures and temperatures. Finally. we show that our model shows transferability to different materials, including iron monophosphide, di-iron phosphide, and three allotropes of

iron metal. Future work can involve further refinement of our Fe/P DFTB model by including training data from additional materials, phases, and thermodynamic state points. Ultimately, our model will help with simulations of prebiotic synthesis, where the role of aqueous schreibersite systems in phosphate production is difficult to discern, and there is subsequently a need for quantum simulations for predictions of chemical and physical properties to help elucidate future experiments.

Acknowledgement

This work was performed under the auspices of the U.S. Department of Energy by Lawrence Livermore National Laboratory under Contract DE-AC52-07NA27344. The authors gratefully thank the Exobiology Program Element NNH20ZDA001N-EXO for support (proposal #20-EXO20-0149).

Supporting Information Available

Additional validation data for all sets of confining radii and ChIMES repulsive energies included in our study.

Data Availability

The SKF interaction files and the ChIMES parameter files for our optimal DFTB/ChIMES model are available in the following public repository: https://github.com/rdettori/dftb_FeP_Erep (last accessed November 6, 2024).

References

- (1) Pasek, M. A.; Gull, M.; Herschy, B. Phosphorylation on the early earth. *Chemical Geology* **2017**, 475, 149 – 170.
- (2) Gulick, A. Phosphorus as a factor in the origin of life. *American Scientist* **1955**, 43, 479–489.
- (3) Pasek, M. A.; Kee, T. P. *Origins of Life: The Primal Self-Organization*; Springer Berlin Heidelberg, 2011; pp 57–84.
- (4) Schwartz, A. W. Phosphorus in prebiotic chemistry. *Philos. Trans. R. Soc. Lond. B Biol. Sci.* **2006**, 361, 1743–1749.
- (5) Pasek, M. A. Schreibersite on the early Earth: Scenarios for prebiotic phosphorylation. *Geoscience Frontiers* **2017**, 8, 329–335.
- (6) Pasek, M. A.; Lauretta, D. A. Aqueous Corrosion of Phosphide Minerals From Iron Meteorites: A Highly Reactive Source of Prebiotic Phosphorus on the Surface of the Early Earth. *Astrobiology* **2005**, 5, 515–535.
- (7) Pasek, M.; Kee, T.; Bryant, D.; Pavlov, A.; Lunine, J. Production of Potentially Prebiotic Condensed Phosphates by Phosphorus Redox Chemistry. *Angewandte Chemie International Edition* **2008**, 47, 7918–7920.
- (8) Gull, M. Prebiotic Phosphorylation Reactions on the Early Earth. *Challenges* **2014**, 5, 193–212.
- (9) Gull, M.; Mojica, M. A.; Fernández, F. M.; Gaul, D. A.; Orlando, T. M.; Liotta, C. L.; Pasek, M. A. Nucleoside phosphorylation by the mineral schreibersite. *Scientific Reports* **2015**, 4, 17198.

(10) Cruz, N. L. L.; Qasim, D.; Abbott-Lyon, H.; Pirim, C.; McKee, A. D.; Orlando, T.; Gull, M.; Lindsaya, D.; Pasek, M. A. The evolution of the surface of the mineral schreibersite in prebiotic chemistry. *Phys. Chem. Chem. Phys.* **2016**, 18, 20160–20167.

(11) Miller, S. L. A production of amino acids under possible primitive Earth conditions. *Science* **1953**, 117, 528.

(12) Manaa, M. R.; Reed, E. J.; Fried, L. E.; Goldman, N. Nitrogen-rich heterocycles as reactivity retardants in shocked insensitive explosives. *J. Am. Chem. Soc.* **2009**, 131, 5493–5487.

(13) Goldman, N.; Reed, E. J.; Fried, L. E.; Kuo, I.-F. W.; Maiti, A. Synthesis of glycine-containing complexes in impacts of comets on early Earth. *Nat. Chem.* **2010**, 2, 949–954.

(14) Goldman, N.; Tamblyn, I. Prebiotic chemistry within a simple impacting icy mixture. *J. Phys. Chem. A* **2013**, 117, 5124 – 5131.

(15) Dettori, R.; Goldman, N. First-Principles Surface Characterization and Water Adsorption of Fe3P Schreibersite. *ACS Earth and Space Chemistry* **2022**, 6, 512–520.

(16) Pantaleone, S.; Corno, M.; Rimola, A.; Balucani, N.; Ugliengo, P. Ab Initio Computational Study on Fe₂NiP Schreibersite: Bulk and Surface Characterization. *ACS Earth and Space Chemistry* **2021**, 5, 1741–1751.

(17) Pantaleone, S.; Corno, M.; Rimola, A.; Balucani, N.; Ugliengo, P. Water Interaction with Fe₂NiP Schreibersite (110) Surface: a Quantum Mechanical Atomistic Perspective. *The Journal of Physical Chemistry C* **2022**, 126, 2243–2252.

(18) Cannella, C.; Goldman, N. Carbyne fiber synthesis within evaporating metallic liquid carbon. *J. Phys. Chem. C* **2015**, 119, 21605–21611.

(19) Lindsey, R. K.; Bastea, S.; Goldman, N.; Fried, L. E. Investigating 3,4-bis(3-nitrofuran-4-yl)furoxan detonation with a rapidly tuned density functional tight binding model. *J. Chem. Phys.* **2021**, 154, 164115.

(20) Armstrong, M. R.; Lindsey, R. K.; Goldman, N.; Nielsen, M. H.; Stavrou, E.; Fried, L. E.; Zaug, J. M.; Bastea, S. Ultrafast shock synthesis of nanocarbon from a liquid precursor. *Nature Communications* **2020**, 11, 353.

(21) Lindsey, R. K.; Goldman, N.; Fried, L. E.; Bastea, S. Chemistry-mediated Ostwald ripening in carbonrich C/O systems at extreme conditions. *Nature Communications* **2022**, 13, 1424.

(22) Nomora, K.; Kalia, R. K.; Nakano, A.; Vashista, P.; van Duin, A. C. T.; Goddard, W. A. Dynamic transition in the shock structure of an energetic material. *Phys. Rev. Lett.* **2007**, 99, 148303.

(23) Drautz, R. Atomic cluster expansion for accurate and transferable interatomic potentials. *Phys. Rev. B* **2019**, 99, 014104.

(24) Smith, J. S.; Nebgen, B. T.; Zubatyuk, R.; Lubbers, N.; Devereux, C.; Barros, K.; Tretiak, S.; Isayev, O.; Roitberg, A. E. Approaching coupled cluster accuracy with a general-purpose neural network potential through transfer learning. *Nat. Commun.* **2019**, 10, 1–8.

(25) Kovács, D. P.; van der Oord, C.; Kucera, J.; Allen, A. E. A.; Cole, D. J.; Ortner, C.; Csányi, G. Linear Atomic Cluster Expansion Force Fields for Organic Molecules: Beyond RMSE. *J. Chem. Theory. Comput.* **2021**, 17, 7696–7711.

(26) Pham, C. H.; Lindsey, R. K.; Fried, L. E.; Goldman, N. Calculation of the detonation state of HN_3 with quantum accuracy. *J. Chem. Phys.* **2021**, 153, 224102.

(27) Elstner, M.; Porezag, D.; Jungnickel, G.; Elsner, J.; Haugk, M.; Frauenheim, T.; Suhai, S.; Seifert, G. Self-consistent-charge density-functional tight-binding method for simulations of complex materials properties. *Phys. Rev. B* **1998**, 58, 7260–7268.

(28) Gaus, M.; Cui, Q.; Elstner, M. DFTB3: Extension of the Self-Consistent-Charge Density-Functional Tight-Binding Method (SCC-DFTB). *Journal of Chemical Theory and Computation* **2011**, 7, 931–948.

(29) Hourahine, B.; Aradi, B.; Blum, V.; Bonafé, F.; Buccheri, A.; Camacho, C.; Cevallos, C.; Deshaye, M. Y.; Dumitrică, T.; Dominguez, A. et al. DFTB+, a software package for efficient approximate density functional theory based atomistic simulations. *The Journal of Chemical Physics* **2020**, 152, 124101.

(30) Goldman, N.; Koziol, L.; Fried, L. E. Using force-matched potentials to improve the accuracy of density functional tight binding for reactive conditions. *J. Chem. Theory Comput.* **2015**, 11, 4530–4535.

(31) Kandy, A. K. A.; Wadbro, E.; Aradi, B.; Broqvist, P.; Kullgren, J. Curvature Constrained Splines for DFTB Repulsive Potential Parametrization. *J. Chem. Theory Comput.* **2021**, 1771-1781, 21.

(32) Wengert, S.; Csányi, G.; Reuter, K.; Margraf, J. T. Data-efficient machine learning for molecular crystal structure prediction. *Chem. Sci.* **2021**, 12, 4536.

(33) Goldman, N.; Fried, L. E.; Lindsey, R. K.; Pham, C. H.; Dettori, R. Enhancing the accuracy of density functional tight binding models through ChIMES many-body interaction potentials. *J. Chem. Phys.* **2023**, 158, 144112.

(34) Stöhr, M.; Medrano Sandonas, L.; Tkatchenko, A. Accurate Many-Body Repulsive Potentials for Density-Functional Tight Binding from Deep Tensor Neural Networks. *J. Phys. Chem. Lett.* **2020**, 11, 6835–6843.

(35) Yang, Y.; Yu, H.; York, D.; Elstner, M.; Cui, Q. Description of Phosphate Hydrolysis Reactions with the Self-Consistent-Charge Density-Functional-Tight-Binding (SCC-DFTB) Theory. 1. Parameterization. *Journal of Chemical Theory and Computation* **2008**, 4, 2067–2084.

(36) Niehaus, T.; Elstner, M.; Frauenheim, T.; Suhai, S. Application of an approximate density-functional method to sulfur containing compounds. *Journal of Molecular Structure: THEOCHEM* **2001**, 541, 185–194.

(37) Guimarães, L.; Enyashin, A. N.; Frenzel, J.; Heine, T.; Duarte, H. A.; Seifert, G. Imogolite Nanotubes: Stability, Electronic, and Mechanical Properties. *ACS Nano* **2007**, 1, 362–368.

(38) Luschnitz, R.; Oliveira, A. F.; Frenzel, J.; Joswig, J.-O.; Seifert, G.; Duarte, H. A. Adsorption of phosphonic and ethylphosphonic acid on aluminum oxide surfaces. *Surface Science* **2008**, 602, 1347–1359.

(39) Sieck, A.; Frauenheim, T.; Jackson, K. A. Shape transition of medium-sized neutral silicon clusters. *physica status solidi (b)* **2003**, 240, 537–548.

(40) Köhler, C.; Seifert, G.; Frauenheim, T. Density functional based calculations for Fen ($n \leq 32$). *Chemical Physics* **2005**, 309, 23–31.

(41) Gaus, M.; Goez, A.; Elstner, M. Parametrization and Benchmark of DFTB3 for Organic Molecules. *Journal of Chemical Theory and Computation* **2012**, 9, 338–354.

(42) Kubillus, M.; Kubař, T.; Gaus, M.; Řezáč, J.; Elstner, M. Parameterization of the DFTB3 Method for Br, Ca, Cl, F, I, K, and Na in Organic and Biological Systems. *Journal of Chemical Theory and Computation* **2014**, 11, 332–342.

(43) Gaus, M.; Lu, X.; Elstner, M.; Cui, Q. Parameterization of DFTB3/3OB for Sulfur and

Phosphorus for Chemical and Biological Applications. Journal of Chemical Theory and Computation **2014**, 10, 1518–1537.

(44) Zheng, G.; Witek, H. A.; Bobadova-Parvanova, P.; Irle, S.; Musaev, D. G.; Prabhakar, R.; Morokuma, K.; Lundberg, M.; Elstner, M.; Köhler, C. et al. Parameter Calibration of Transition-Metal Elements for the Spin-Polarized Self-Consistent-Charge Density-Functional Tight-Binding (DFTB) Method: Sc, Ti, Fe, Co, and Ni. Journal of Chemical Theory and Computation **2007**, 3, 1349–1367.

(45) Lindsey, R. K.; Goldman, N.; Fried, L. E.; Bastea, S. Many-body reactive force field development for carbon condensation in C/O systems under extreme conditions. The Journal of Chemical Physics **2020**, 153, 054103.

(46) Lindsey, R. K.; Fried, L. E.; Goldman, N.; Bastea, S. Active learning for robust, high-complexity reactive atomistic simulations. The Journal of Chemical Physics **2020**, 153, 134117.

(47) Goldman, N.; Fried, L. E.; Lindsey, R. K.; Pham, C. H.; Dettori, R. Enhancing the accuracy of density functional tight binding models through ChIMES many-body interaction potentials. The Journal of Chemical Physics **2023**, 158, 144112.

(48) Goldman, N.; Kweon, K. E.; Sadigh, B.; Heo, T.-W.; Lindsey, R. K.; Pham, C. H.; Fried, L. E.; Aradi, B.; Holliday, K.; Jeffries, J. R. et al. Semi-Automated Creation of Density Functional Tight Binding Models through Leveraging Chebyshev Polynomial-Based Force Fields. J. Chem. Theory Comput. **2021**, 17, 4435–4448.

(49) Goldman, N.; Aradi, B.; Lindsey, R. K.; Fried, L. E. Development of a Multicenter Density Functional Tight Binding Model for Plutonium Surface Hydriding. J. Chem. Theory. Comput. **2018**, 14, 2652–2660.

(50) Pham, C. H.; Linsel, R. K.; Fried, L. E.; Goldman, N. High-Accuracy Semiempirical

Quantum Models Based on a Minimal Training Set. *J. Phys. Chem. Lett.* **2022**, 13, 2934–2942.

- (51) Kresse, G.; Hafner, J. Ab initio molecular dynamics for liquid metals. *Phys. Rev. B* **1993**, 47, 558–561.
- (52) Kresse, G.; Hafner, J. Ab initio molecular-dynamics simulation of the liquid-metal–amorphous-semiconductor transition in germanium. *Phys. Rev. B* **1994**, 49, 14251–14269.
- (53) Kresse, G.; Furthmüller, J. Efficient iterative schemes for ab initio total-energy calculations using a plane-wave basis set. *Phys. Rev. B* **1996**, 54, 11169–11186.
- (54) Kresse, G.; Joubert, D. From ultrasoft pseudopotentials to the projector augmented-wave method. *Phys. Rev. B* **1999**, 59, 1758–1775.
- (55) Blöchl, P. E. Projector augmented-wave method. *Phys. Rev. B* **1994**, 50, 17953–17979.
- (56) Perdew, J. P.; Burke, K.; Ernzerhof, M. Generalized Gradient Approximation Made Simple. *Phys. Rev. Lett.* **1996**, 77, 3865–3868.
- (57) Methfessel, M.; Paxton, A. T. High-precision sampling for Brillouin-zone integration in metals. *Phys. Rev. B* **1989**, 40, 3616–3621.
- (58) Monkhorst, H. J.; Pack, J. D. Special points for Brillouin-zone integrations. *Phys. Rev. B* **1976**, 13, 5188–5192.
- (59) Bedolla, P. O.; Feldbauer, G.; Wolloch, M.; Eder, S. J.; Dörr, N.; Mohn, P.; Redinger, J.; Vernes, A. Effects of van der Waals Interactions in the Adsorption of Isooctane and Ethanol on Fe(100) Surfaces. *The Journal of Physical Chemistry C* **2014**, 118, 17608–17615.

(60) Elstner, M.; Porezag, D.; Jungnickel, G.; Elsner, J.; Haugk, M.; Frauenheim, T.; Suhai, S.; Seifert, G. Self-consistent-charge density-functional tight-binding method for simulations of complex materials properties. *Physical Review B* **1998**, 58, 7260–7268.

(61) Aradi, B.; Hourahine, B.; Frauenheim, T. DFTB+, a sparse matrix-based implementation of the DFTB method. *J. Phys. Chem. A* **2007**, 111, 5678–5684.

(62) Koskinen, P.; Mäkinen, V. Density-functional tight-binding for beginners. *Comp. Mater. Sci.* **2009**, 47, 237–253.

(63) Gaus, M.; Cui, Q.; Elstner, M. DFTB3: Extension of the Self-Consistent-Charge Density-Functional Tight-Binding Method (SCC-DFTB). *J. Chem. Theory Comput.* **2011**, 7, 931–948.

(64) Vuong, V. Q.; Madridejos, J. M. L.; Aradi, B.; Sumpter, B. G.; Metha, G. F.; Irle, S. Density-functional tight-binding for phosphine-stabilized nanoscale gold clusters. *Chemical Science* **2020**, 11, 13113–13128.

(65) Dantanarayana, V.; Nemataram, T.; Vong, D.; Anthony, J. E.; Troisi, A.; Cong, K. N.; Goldman, N.; Faller, R.; Moulé, A. J. Predictive Model of Charge Mobilities in Organic Semiconductor Small Molecules with Force-Matched Potentials. *Journal of Chemical Theory and Computation* **2020**, 16, 3494–3503.

(66) Chou, C.-P.; Nishimura, Y.; Fan, C.-C.; Mazur, G.; Irle, S.; Witek, H. A. Automated parameterization of DFTB using particle swarm optimization. *J. Chem. Theory Comput.* **2016**, 12, 53–64.

(67) Goldman, N.; Kweon, K. E.; Sadigh, B.; Heo, T. W.; Lindsey, R. K.; Pham, C. H.; Fried, L. E.; Aradi, B.; Holliday, K.; Jeffries, J. R. et al. Semi-Automated Creation of Density Functional Tight Binding Models through Leveraging Chebyshev Polynomial-Based Force Fields. *Journal of Chemical Theory and Computation* **2021**, 17, 4435–4448.

(68) Cui, M.; Reuter, K.; Margraf, J. Obtaining Robust Density Functional Tight-Binding Parameters for Solids across the Periodic Table. *J. Chem. Theory Comput.* **2024**, 20, 5276–5290.

(69) Tersoff, J. Empirical interatomic potential for carbon, with application to amorphous-carbon. *Phys. Rev. Lett.* **1988**, 61, 2879.

(70) Vinet, P.; Smith, J. R.; Ferrante, J.; Rose, J. H. Temperature effects on the universal equation of state of solids. *Physical Review B* **1987**, 35, 1945–1953.

(71) High-pressure behavior of Fe_3P and the role of phosphorus in planetary cores. *Earth and Planetary Science Letters* **2014**, 390, 296–303.

(72) Scott, H. P.; Huggins, S.; Frank, M. R.; Maglio, S. J.; Martin, C. D.; Meng, Y.; Santillán, J.; Williams, Q. Equation of state and high-pressure stability of Fe_3P -schreibersite: Implications for phosphorus storage in planetary cores. *Geophysical Research Letters* **2007**, 34, L06302.

(73) <https://pymatgen.org> (last accessed November 7, 2024).

(74) Scott, H.; Kiefer, B.; Martin, C. D.; Boateng, N.; Frank, M.; Meng, Y. P-V equation of state for Fe_2P and pressure-induced phase transition in Fe_3P . *High Pressure Research* **2008**, 28, 375–384.

(75) Togo, A.; Chaput, L.; Tadano, T.; Tanaka, I. Implementation strategies in phonopy and phono3py. *J. Phys. Condens. Matter* **2023**, 35, 353001.

(76) Togo, A. First-principles Phonon Calculations with Phonopy and Phono3py. *J. Phys. Soc. Jpn.* **2023**, 92, 012001.

(77) Chernyavskii, I. O.; Nikitin, S. E.; Onykiienko, Y. A.; Inosov, D. S.; Stahl, Q.; Geck, J.; Hong, X. C.; Hess, C.; Gass, S.; Wolter, A. U. B. et al. Incommensurate magnet iron

monophosphide FeP: Crystal growth and characterization. Physical Review Materials **2020**, 4.

(78) Huang, H.; Yu, C.; Yang, J.; Han, X.; Zhao, C.; Li, S.; Liu, Z.; Qiu, J. Ultrasmall diiron phosphide nanodots anchored on graphene sheets with enhanced electrocatalytic activity for hydrogen production via high-efficiency water splitting. Journal of Materials Chemistry A **2016**, 4, 16028–16035.

(79) Dera, P.; Lavina, B.; Borkowski, L. A.; Prakapenka, V. B.; Sutton, S. R.; Rivers, M. L.; Downs, R. T.; Boctor, N. Z.; Prewitt, C. T. High-pressure polymorphism of Fe_2P and its implications for meteorites and Earth's core. Geophysical Research Letters **2008**, 35, L10301.

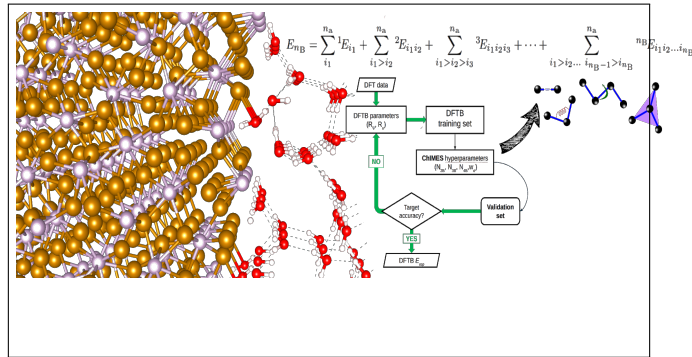
(80) Mathon, O.; Baudelet, F.; Itié, J. P.; Polian, A.; d'Astuto, M.; Chervin, J. C.; Pascarelli, S. Dynamics of the Magnetic and Structural $\alpha - \epsilon$ Phase Transition in Iron. Physical Review Letters **2004**, 93, 255503.

(81) Introductory Chemistry for the Environmental Sciences; Cambridge University Press, 1996; pp 148–209.

(82) SEKI, I.; NAGATA, K. Lattice Constant of Iron and Austenite Including Its Supersaturation Phase of Carbon. ISIJ International **2005**, 45, 1789–1794.

(83) Takahashi, T.; Bassett, W. A.; Mao, H.-K. Isothermal compression of the alloys of iron up to 300 kilobars at room temperature: Iron-nickel alloys. Journal of Geophysical Research **1968**, 73, 4717–4725.

TOC Graphic



Supplementary Information: Creation of an Fe_3P Schreibersite Density Functional Tight Binding Model for Astrobiological Simulations

Riccardo Dettori^{*,†} and Nir Goldman^{*,†,‡}

[†]*Physical and Life Sciences Directorate, Lawrence Livermore National Laboratory, 7000 East Avenue, Livermore, California 94550, United States*

[‡]*Department of Chemical Engineering, University of California, Davis, California 95616, United States*

E-mail: dettori1@llnl.gov; ngoldman@llnl.gov

Root-mean-squared errors (RMSE) for forces and stress tensor

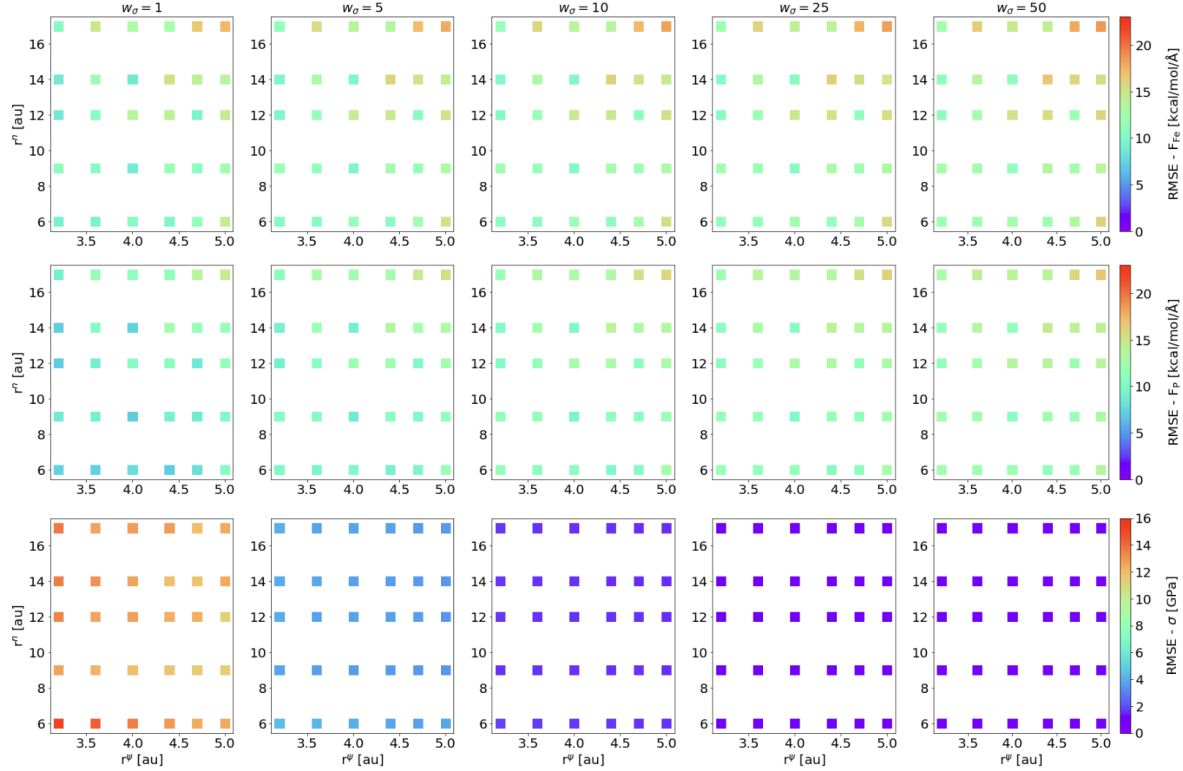


Figure S1: RMSE for the $\{8,4,0\}$ set. Top panel: forces on iron atoms, central panel: forces on phosphorous atoms, bottom panel: stress tensor.

Table S1: RMSE for the $\{8,4,0\}$ set. RMSE on forces are expressed in kcal/mol/Å, RMSE on stress tensor components are expressed in GPa

R_Ψ	R_n	$w_\sigma = 0$				$w_\sigma = 5$				$w_\sigma = 10$				$w_\sigma = 25$				$w_\sigma = 50$			
		Fe	P	σ	Fe	P	σ	Fe	P	σ	Fe	P	σ	Fe	P	σ	Fe	P	σ		
3.2	6	9.223	7.288	15.219	10.318	9.991	4.455	10.801	11.184	1.824	11.162	11.762	1.171	11.803	12.377	0.997					
3.2	9	10.901	8.743	12.671	11.683	10.387	3.787	12.015	11.199	1.669	12.262	11.649	1.15	12.778	12.256	0.981					
3.2	12	8.711	7.014	13.389	9.803	9.157	3.965	10.239	10.15	1.698	10.526	10.678	1.144	11.078	11.33	0.981					
3.2	14	8.689	7.043	13.565	9.793	9.229	3.995	10.234	10.232	1.7	10.519	10.759	1.141	11.06	11.396	0.979					
3.2	17	10.323	9.108	13.701	11.281	10.908	4.028	11.679	11.78	1.704	11.937	12.24	1.139	12.421	12.797	0.978					
3.6	6	9.426	7.237	14.388	10.441	9.688	4.241	10.888	10.783	1.778	11.244	11.336	1.169	11.902	11.983	0.991					
3.6	9	10.446	9.024	12.203	11.279	10.457	3.648	11.618	11.186	1.639	11.877	11.606	1.147	12.427	12.214	0.977					
3.6	12	10.583	9.005	12.578	11.389	10.559	3.747	11.723	11.335	1.659	11.96	11.778	1.151	12.469	12.375	0.987					
3.6	14	12.008	10.314	13.114	12.812	11.776	3.858	13.138	12.519	1.67	13.371	12.929	1.137	13.828	13.468	0.971					
3.6	17	15.031	11.463	12.682	15.629	12.746	3.779	15.882	13.412	1.649	16.063	13.788	1.129	16.415	14.294	0.966					
4	6	10.537	7.909	13.519	11.38	9.953	4.018	11.755	10.899	1.733	12.076	11.407	1.167	12.697	12.066	0.985					
4	9	8.893	7.034	11.912	9.827	8.739	3.582	10.203	9.565	1.631	10.497	10.048	1.149	11.121	10.765	0.975					
4	12	13.788	10.612	12.69	14.443	11.979	3.767	14.718	12.677	1.651	14.914	13.074	1.132	15.31	13.609	0.967					
4	14	8.74	7.22	12.6	9.756	9.069	3.717	10.151	9.943	1.643	10.432	10.431	1.137	11	11.098	0.97					
4	17	12.983	11.106	12.855	13.727	12.419	3.805	14.03	13.102	1.664	14.25	13.492	1.137	14.686	14.024	0.967					
4.4	6	9.761	7.034	12.897	10.648	9.057	3.823	11.027	9.973	1.69	11.368	10.478	1.162	12.053	11.185	0.98					
4.4	9	11.757	9.26	11.721	12.453	10.572	3.528	12.741	11.241	1.631	12.978	11.65	1.16	13.51	12.273	0.986					
4.4	12	14.067	10.891	12.364	14.689	12.158	3.69	14.949	12.811	1.649	15.157	13.199	1.143	15.588	13.763	0.967					
4.4	14	15.349	12.427	11.866	15.966	13.438	3.566	16.211	13.98	1.622	16.406	14.316	1.137	16.805	14.836	0.962					
4.4	17	12.625	11.117	12.757	13.409	12.404	3.754	13.719	13.064	1.655	13.941	13.447	1.139	14.387	13.984	0.969					
4.7	6	11.33	8.07	12.417	12.107	9.739	3.709	12.433	10.539	1.67	12.753	10.99	1.162	13.396	11.666	0.978					
4.7	9	10.768	8.759	11.445	11.478	10.075	3.475	11.773	10.748	1.628	12.026	11.179	1.166	12.603	11.858	0.988					
4.7	12	9.648	8.593	12.333	10.582	10.121	3.662	10.952	10.88	1.646	11.224	11.322	1.146	11.836	11.962	0.97					
4.7	14	14.439	11.578	11.711	15.063	12.631	3.505	15.308	13.187	1.608	15.495	13.538	1.136	15.889	14.084	0.962					
4.7	17	16.601	13.84	11.902	17.176	14.747	3.539	17.4	15.236	1.614	17.574	15.54	1.136	17.935	16.007	0.966					
5	6	14.448	10.439	12.482	15.14	11.773	3.751	15.427	12.462	1.685	15.699	12.857	1.162	16.248	13.445	0.971					
5	9	12.221	10.151	11.383	12.858	11.282	3.43	13.114	11.87	1.622	13.315	12.264	1.168	13.812	12.888	0.991					
5	12	14.497	11.333	11.374	15.112	12.335	3.434	15.353	12.872	1.61	15.554	13.229	1.146	15.981	13.82	0.963					
5	14	13.834	11.687	12.455	14.53	12.828	3.478	14.774	13.354	1.598	14.968	13.688	1.145	15.408	14.238	0.968					
5	17	17.429	14.519	12.444	18.009	15.454	3.523	18.216	15.917	1.613	18.367	16.216	1.143	18.702	16.7	0.964					

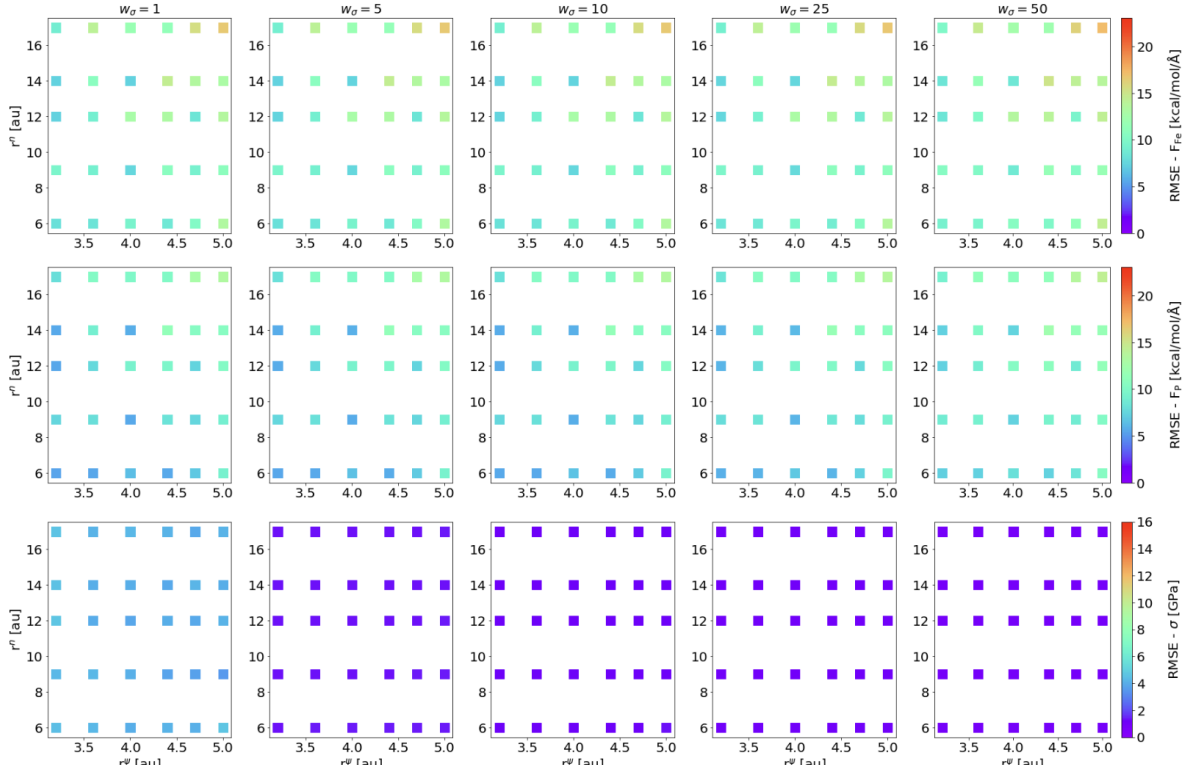


Figure S2: RMSE for the $\{12,8,0\}$ set. Top panel: forces on iron atoms, central panel: forces on phosphorous atoms, bottom panel: stress tensor.

Table S2: RMSE for the {12,8,0} set. RMSE on forces are expressed in kcal/mol/Å, RMSE on stress tensor components are expressed in GPa

R_{Ψ}	R_n	$w_{\sigma}=0$				$w_{\sigma}=5$				$w_{\sigma}=10$				$w_{\sigma}=25$				$w_{\sigma}=50$			
		Fe	P	σ	Fe	P	σ	Fe	P	σ	Fe	P	σ	Fe	P	σ	Fe	P	σ		
3.2	6	8.083	5.436	4.476	8.101	5.561	1.372	8.119	5.588	1.279	8.366	5.915	1.114	9.35	7.172	0.905					
3.2	9	9.648	7.537	4.272	9.653	7.617	1.35	9.655	7.641	1.266	9.796	7.892	1.108	10.523	8.861	0.909					
3.2	12	7.358	5.566	4.647	7.393	5.684	1.349	7.398	5.719	1.254	7.573	6.054	1.098	8.458	7.253	0.903					
3.2	14	7.325	5.586	4.545	7.353	5.689	1.339	7.356	5.723	1.248	7.525	6.059	1.095	8.402	7.252	0.901					
3.2	17	8.983	7.994	4.617	9.011	8.063	1.339	9.014	8.086	1.246	9.167	8.323	1.092	9.926	9.219	0.9					
3.6	6	8.29	5.522	4.259	8.305	5.63	1.376	8.325	5.655	1.288	8.581	5.983	1.12	9.574	7.241	0.908					
3.6	9	9.139	7.969	4.267	9.165	8.028	1.357	9.172	8.048	1.272	9.35	8.295	1.11	10.176	9.215	0.911					
3.6	12	9.076	7.682	3.965	9.098	7.735	1.348	9.101	7.758	1.27	9.248	8.015	1.114	10.011	8.972	0.919					
3.6	14	10.724	9.06	4	10.748	9.103	1.332	10.754	9.121	1.252	10.901	9.332	1.095	11.58	10.148	0.9					
3.6	17	14.1	10.356	4.183	14.113	10.405	1.325	14.12	10.421	1.238	14.224	10.603	1.084	14.697	11.307	0.894					
4	6	9.466	6.486	4.058	9.476	6.574	1.382	9.492	6.594	1.297	9.715	6.892	1.123	10.607	8.029	0.909					
4	9	7.572	5.673	4.115	7.597	5.758	1.361	7.606	5.787	1.278	7.821	6.126	1.114	8.781	7.354	0.909					
4	12	12.849	9.394	3.858	12.869	9.438	1.326	12.873	9.456	1.247	12.986	9.657	1.089	13.53	10.433	0.897					
4	14	7.371	5.824	4.059	7.401	5.901	1.336	7.407	5.929	1.255	7.595	6.253	1.097	8.505	7.428	0.899					
4	17	11.815	9.956	4.265	11.839	10.002	1.346	11.846	10.021	1.258	11.982	10.224	1.095	12.609	10.984	0.897					
4.4	6	8.628	5.612	4.137	8.644	5.713	1.387	8.667	5.735	1.299	8.932	6.069	1.124	9.924	7.325	0.909					
4.4	9	10.731	8.228	3.781	10.744	8.269	1.371	10.749	8.288	1.296	10.901	8.541	1.128	11.62	9.478	0.923					
4.4	12	13.2	9.752	4.047	13.217	9.804	1.357	13.225	9.822	1.271	13.354	10.026	1.105	13.93	10.82	0.9					
4.4	14	14.436	11.39	3.884	14.458	11.426	1.359	14.464	11.441	1.275	14.589	11.622	1.103	15.126	12.316	0.897					
4.4	17	11.426	10.16	4.182	11.452	10.2	1.349	11.458	10.217	1.266	11.596	10.421	1.102	12.247	11.186	0.9					
4.7	6	10.242	6.87	4.081	10.271	6.95	1.394	10.29	6.969	1.303	10.518	7.247	1.125	11.394	8.319	0.909					
4.7	9	9.294	7.49	3.744	9.31	7.537	1.382	9.317	7.56	1.307	9.497	7.845	1.135	10.329	8.882	0.926					
4.7	12	8.425	7.419	3.902	8.452	7.469	1.357	8.462	7.49	1.278	8.664	7.76	1.11	9.56	8.763	0.903					
4.7	14	13.482	10.519	4.195	13.507	10.564	1.359	13.512	10.581	1.27	13.63	10.783	1.099	14.164	11.526	0.895					
4.7	17	15.57	12.857	3.902	15.595	12.88	1.348	15.601	12.892	1.267	15.711	13.053	1.099	16.205	13.65	0.899					
5	6	13.384	9.341	4.651	13.409	9.421	1.424	13.426	9.439	1.317	13.62	9.662	1.13	14.341	10.501	0.909					
5	9	10.934	9.037	3.556	10.949	9.072	1.384	10.95	9.092	1.311	10.075	9.341	1.138	11.754	10.232	0.931					
5	12	13.586	10.299	4.176	13.609	10.344	1.384	13.615	10.362	1.295	13.745	10.581	1.113	14.302	11.375	0.899					
5	14	12.98	10.624	4.009	13.02	10.655	1.37	13.027	10.671	1.284	13.159	10.873	1.111	13.747	11.635	0.904					
5	17	16.624	13.393	4.14	16.661	13.421	1.376	16.663	13.436	1.29	16.746	13.606	1.11	17.189	14.242	0.9					

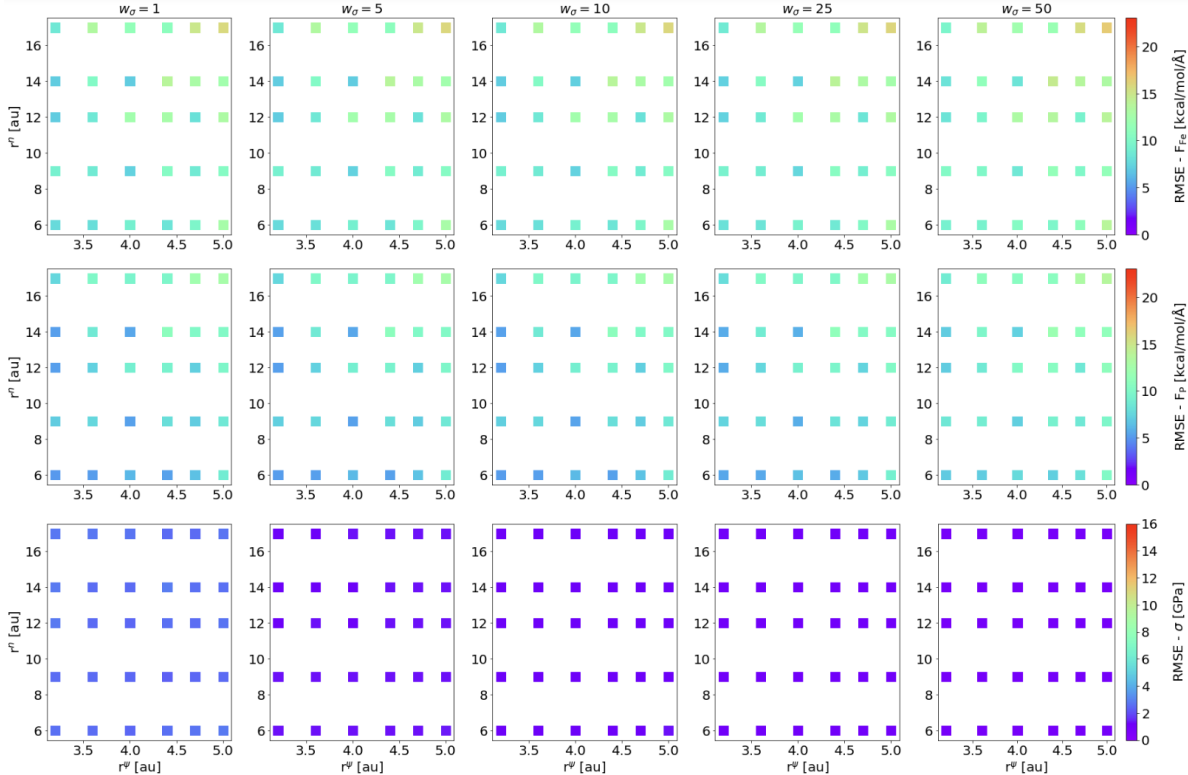


Figure S3: RMSE for the {16,12,0} set. Top panel: forces on iron atoms, central panel: forces on phosphorous atoms, bottom panel: stress tensor.

Table S3: RMSE for the {16,12,0} set. RMSE on forces are expressed in kcal/mol/Å, and RMSE on stress tensor components are expressed in GPa

R_Ψ	R_n	$w_\sigma=0$				$w_\sigma=5$				$w_\sigma=10$				$w_\sigma=25$				$w_\sigma=50$			
		Fe	P	σ	Fe	P	σ	Fe	P	σ	Fe	P	σ	Fe	P	σ	Fe	P	σ		
3.2	6	7.806	5.113	2.679	7.81	5.135	1.333	7.83	5.153	1.281	8.121	5.533	1.103	9.19	6.958	0.873					
3.2	9	9.241	7.104	2.625	9.245	7.123	1.315	9.249	7.139	1.264	9.433	7.423	1.094	10.257	8.505	0.875					
3.2	12	7.092	5.261	2.86	7.1	5.287	1.309	7.103	5.312	1.255	7.317	5.692	1.087	8.311	7.051	0.87					
3.2	14	7.065	5.288	2.817	7.077	5.317	1.303	7.079	5.341	1.25	7.286	5.717	1.084	8.268	7.068	0.868					
3.2	17	8.592	7.613	2.77	8.601	7.631	1.303	8.607	7.647	1.25	8.803	7.899	1.084	9.675	8.898	0.869					
3.6	6	8.015	5.214	2.576	8.02	5.232	1.341	8.042	5.249	1.289	8.34	5.627	1.108	9.411	7.044	0.875					
3.6	9	8.746	7.614	2.54	8.755	7.625	1.327	8.764	7.639	1.275	8.983	7.899	1.101	9.91	8.925	0.879					
3.6	12	8.594	7.256	2.546	8.602	7.268	1.322	8.605	7.285	1.272	8.789	7.568	1.102	9.652	8.652	0.884					
3.6	14	10.257	8.665	2.572	10.265	8.674	1.312	10.274	8.686	1.262	10.457	8.916	1.09	11.253	9.834	0.87					
3.6	17	13.383	9.953	2.804	13.386	9.964	1.302	13.392	9.977	1.249	13.521	10.186	1.078	14.085	11.001	0.862					
4	6	9.172	6.215	2.479	9.175	6.228	1.35	9.193	6.242	1.298	9.452	6.574	1.111	10.417	7.834	0.875					
4	9	7.314	5.387	2.497	7.322	5.403	1.332	7.332	5.425	1.28	7.589	5.804	1.102	8.642	7.178	0.876					
4	12	12.361	9.052	2.484	12.364	9.06	1.308	12.37	9.073	1.258	12.514	9.302	1.084	13.143	10.192	0.865					
4	14	7.109	5.533	2.518	7.116	5.548	1.308	7.122	5.569	1.259	7.354	5.933	1.087	8.372	7.256	0.866					
4	17	11.387	9.553	2.701	11.393	9.563	1.325	11.402	9.575	1.271	11.584	9.793	1.092	12.316	10.646	0.867					
4.4	6	8.349	5.341	2.642	8.356	5.361	1.355	8.381	5.376	1.3	8.69	5.755	1.111	9.75	7.154	0.874					
4.4	9	10.421	7.969	2.333	10.427	7.975	1.354	10.435	7.991	1.303	10.62	8.271	1.118	11.398	9.31	0.89					
4.4	12	12.717	9.408	2.671	12.722	9.421	1.339	12.733	9.434	1.285	12.908	9.667	1.1	13.59	10.565	0.868					
4.4	14	13.804	10.903	2.904	13.814	10.914	1.345	13.823	10.926	1.286	13.98	11.128	1.096	14.611	11.912	0.864					
4.4	17	10.951	9.735	2.532	10.957	9.744	1.321	10.966	9.756	1.268	11.141	9.965	1.09	11.876	10.794	0.868					
4.7	6	9.796	6.567	2.706	9.809	6.585	1.363	9.831	6.595	1.306	10.111	6.905	1.111	11.071	8.105	0.874					
4.7	9	8.823	7.074	2.444	8.832	7.086	1.361	8.839	7.103	1.308	9.055	7.419	1.121	9.981	8.58	0.891					
4.7	12	8.168	7.15	2.608	8.179	7.163	1.336	8.19	7.179	1.282	8.438	7.47	1.098	9.426	8.581	0.869					
4.7	14	12.918	10.047	2.684	12.928	10.058	1.331	12.935	10.071	1.272	13.078	10.289	1.086	13.685	11.122	0.859					
4.7	17	14.9	12.291	2.508	14.91	12.297	1.324	14.917	12.305	1.27	15.056	12.472	1.088	15.616	13.145	0.866					
5	6	12.788	8.892	2.814	12.797	8.905	1.386	12.816	8.916	1.326	13.043	9.168	1.122	13.812	10.137	0.879					
5	9	10.431	8.6	2.507	10.44	8.609	1.367	10.441	8.627	1.312	10.601	8.903	1.122	11.357	9.897	0.894					
5	12	13.121	9.882	2.715	13.131	9.898	1.358	13.139	9.912	1.297	13.3	10.146	1.1	13.935	11.026	0.864					
5	14	12.371	10.122	2.666	12.387	10.128	1.341	12.393	10.141	1.285	12.55	10.364	1.096	13.21	11.203	0.868					
5	17	15.854	12.722	2.731	15.869	12.729	1.349	15.872	12.739	1.29	15.986	12.924	1.096	16.506	13.621	0.863					

Table S4: RMSE for the {12,8,4} set. RMSE on forces are expressed in kcal/mol/Å, and RMSE on stress tensor components are expressed in GPa

R_Ψ	R_n	$w_\sigma=0$				$w_\sigma=5$				$w_\sigma=10$				$w_\sigma=25$			
		Fe	P	σ	Fe	P	σ	Fe	P	σ	Fe	P	σ	Fe	P	σ	
3.2	6	7.985	5.197	4.026	8.003	5.277	1.346	8.021	5.303	1.273							
3.2	9	9.564	7.247	3.357	9.56	7.277	1.319	9.564	7.297	1.256							
3.2	12	7.277	5.306	4.236	7.294	5.369	1.312	7.3	5.398	1.237							
3.2	14	7.249	5.316	4.154	7.26	5.373	1.301	7.266	5.399	1.23							
3.2	17	8.924	7.792	4.218	8.94	7.827	1.302	8.946	7.848	1.227							
3.6	6	8.18	5.279	3.83	8.193	5.346	1.353	8.213	5.368	1.281							
3.6	9	9.064	7.774	3.984	9.078	7.807	1.329	9.087	7.826	1.256							
3.6	12	9.002	7.427	3.617	9.007	7.449	1.312	9.011	7.469	1.251							
3.6	14	10.63	8.815	3.668	10.644	8.837	1.305	10.651	8.855	1.238							
3.6	17	13.898	10.053	3.651	13.905	10.082	1.297	13.917	10.094	1.229							
4	6	9.349	6.273	3.628	9.358	6.323	1.358	9.373	6.344	1.288							
4	9	7.485	5.403	3.735	7.496	5.449	1.333	7.509	5.474	1.265							
4	12	12.737	9.148	3.581	12.749	9.174	1.301	12.758	9.188	1.236							
4	14	7.284	5.543	3.836	7.295	5.592	1.306	7.304	5.617	1.24							
4	17	11.72	9.714	3.939	11.736	9.741	1.318	11.743	9.755	1.245							
4.4	6	8.5	5.358	3.702	8.513	5.409	1.361	8.534	5.432	1.289							
4.4	9	10.621	8.011	3.521	10.628	8.034	1.347	10.636	8.053	1.28							
4.4	12	13.098	9.493	3.77	13.107	9.524	1.332	13.116	9.538	1.262							
4.4	14	14.227	11.066	3.421	14.242	11.081	1.334	14.254	11.096	1.269							
4.4	17	11.297	9.912	4.028	11.318	9.936	1.321	11.328	9.952	1.248							
4.7	6	10.103	6.646	3.627	10.122	6.685	1.366	10.142	6.706	1.293							
4.7	9	9.199	7.228	3.289	9.205	7.252	1.35	9.214	7.273	1.288							
4.7	12	8.326	7.152	3.684	8.345	7.182	1.327	8.358	7.2	1.259							
4.7	14	13.318	10.151	3.73	13.328	10.173	1.336	13.338	10.189	1.266							
4.7	17	15.379	12.5	3.249	15.39	12.505	1.338	15.402	12.518	1.271							
5	6	13.092	9.038	4.013	13.109	9.08	1.396	13.127	9.095	1.314							
5	9	10.806	8.781	3.26	10.813	8.806	1.355	10.815	8.826	1.289							
5	12	13.42	9.966	3.709	13.426	9.987	1.356	13.438	10.003	1.284							
5	14	12.728	10.292	3.793	12.756	10.312	1.337	12.766	10.328	1.266</td							

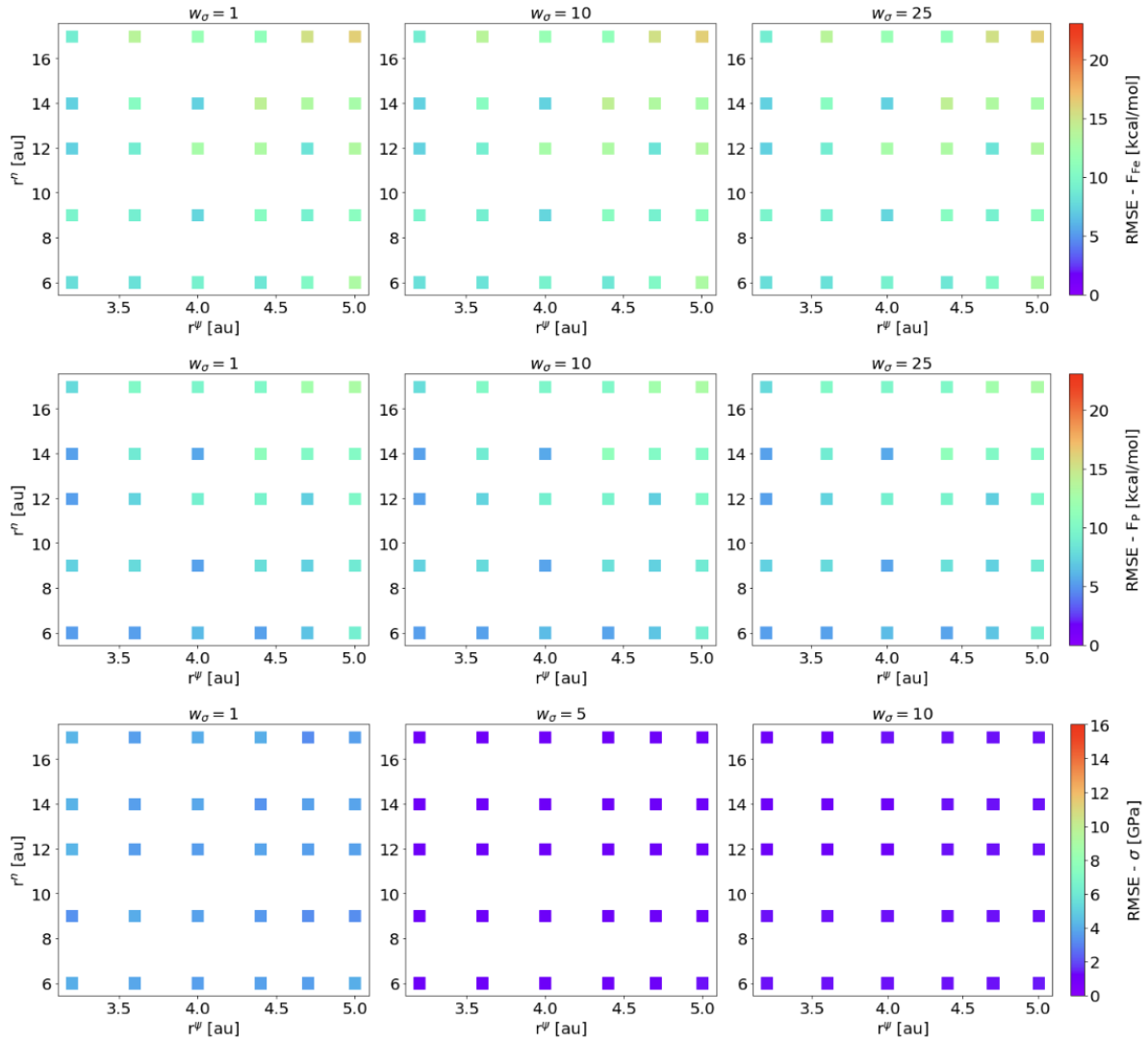


Figure S4: RMSE for the $\{12,8,4\}$ set. Top panel: forces on iron atoms, central panel: forces on phosphorous atoms, bottom panel: stress tensor.

Lattice constants

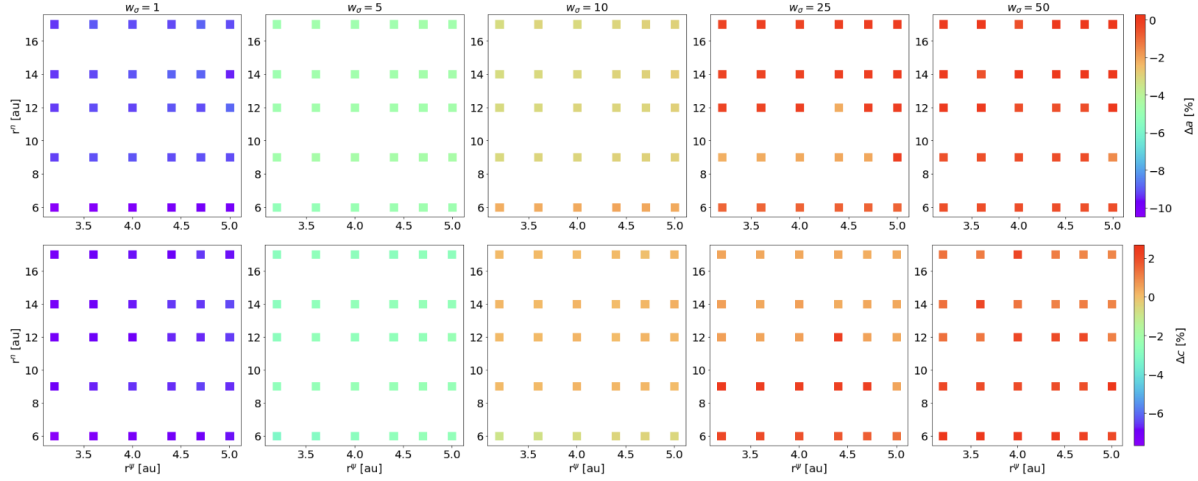


Figure S5: Percentage deviation from DFT values of schreibersite lattice constant for the $\{8,4,0\}$ set. Top panel: lattice constant a , bottom panel: lattice constant c .

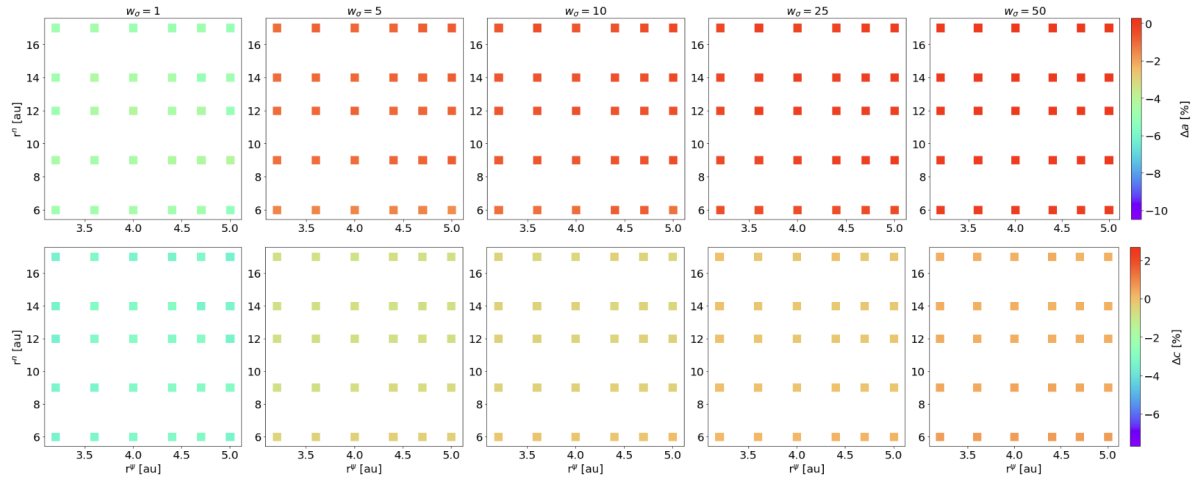


Figure S6: Percentage deviation from DFT values of schreibersite lattice constant for the $\{12,8,0\}$ set. Top panel: lattice constant a , bottom panel: lattice constant c .

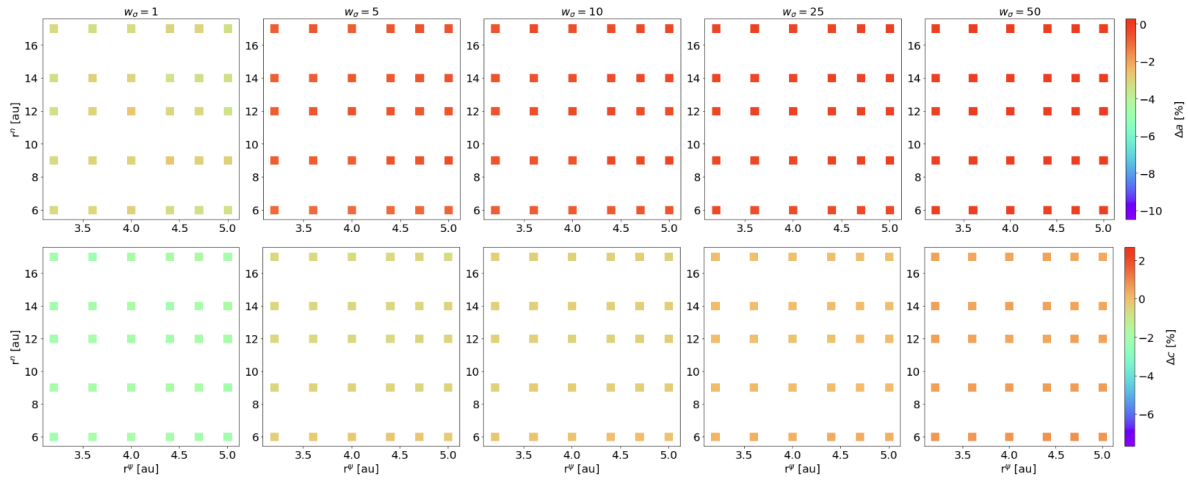


Figure S7: Percentage deviation from DFT values of schreibersite lattice constant for the $\{16,12,0\}$ set. Top panel: lattice constant a , bottom panel: lattice constant c .

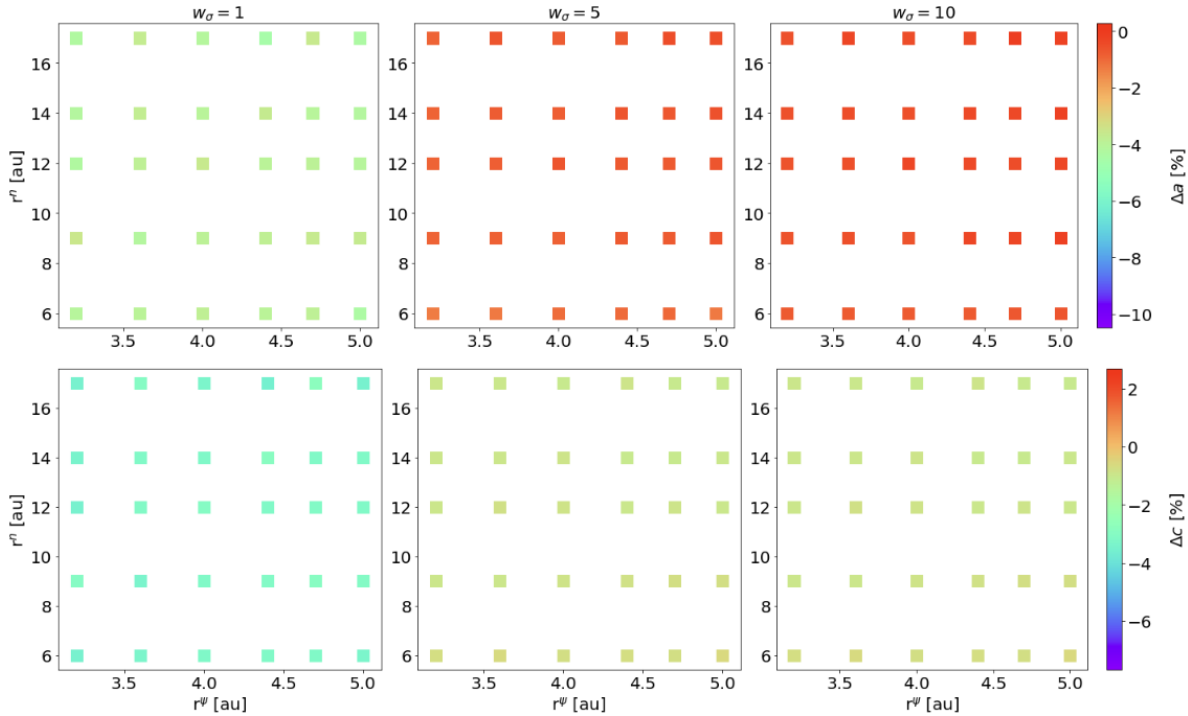


Figure S8: Percentage deviation from DFT values of schreibersite lattice constant for the $\{12,8,4\}$ set. Top panel: lattice constant a , bottom panel: lattice constant c .

Table S5: Lattice constants value for $w_\sigma = 1$ set.

R_Ψ	R_n	a [Å]					c [Å]		
		{8,4,0}	{12,8,0}	{16,12,0}	{12,8,4}	{8,4,0}	{12,8,0}	{16,12,0}	{12,8,4}
3.2	6	8.098	8.611	8.759	8.676	4.044	4.229	4.286	4.228
3.2	9	8.211	8.641	8.759	8.724	4.076	4.234	4.293	4.249
3.2	12	8.205	8.609	8.744	8.660	4.068	4.228	4.284	4.228
3.2	14	8.203	8.617	8.749	8.667	4.067	4.231	4.286	4.230
3.2	17	8.202	8.612	8.758	8.663	4.066	4.228	4.287	4.227
3.6	6	8.113	8.623	8.767	8.687	4.054	4.236	4.292	4.235
3.6	9	8.224	8.636	8.775	8.670	4.085	4.235	4.294	4.232
3.6	12	8.221	8.653	8.774	8.697	4.081	4.243	4.292	4.243
3.6	14	8.216	8.658	8.778	8.705	4.078	4.246	4.295	4.241
3.6	17	8.232	8.629	8.749	8.709	4.079	4.241	4.284	4.248
4	6	8.128	8.636	8.777	8.700	4.064	4.241	4.296	4.240
4	9	8.228	8.642	8.776	8.693	4.091	4.243	4.297	4.241
4	12	8.215	8.673	8.805	8.721	4.077	4.249	4.291	4.248
4	14	8.227	8.642	8.773	8.684	4.083	4.245	4.299	4.240
4	17	8.222	8.605	8.756	8.674	4.082	4.232	4.294	4.234
4.4	6	8.141	8.620	8.756	8.689	4.071	4.243	4.294	4.242
4.4	9	8.222	8.661	8.800	8.701	4.089	4.248	4.299	4.244
4.4	12	8.227	8.638	8.766	8.687	4.087	4.245	4.289	4.241
4.4	14	8.243	8.637	8.732	8.713	4.093	4.251	4.285	4.254
4.4	17	8.219	8.604	8.776	8.636	4.080	4.230	4.298	4.224
4.7	6	8.152	8.620	8.746	8.696	4.075	4.245	4.290	4.242
4.7	9	8.226	8.663	8.785	8.719	4.096	4.248	4.296	4.252
4.7	12	8.221	8.654	8.763	8.693	4.087	4.248	4.295	4.244
4.7	14	8.244	8.584	8.743	8.680	4.092	4.232	4.296	4.242
4.7	17	8.243	8.613	8.772	8.722	4.093	4.239	4.303	4.257
5	6	8.151	8.568	8.741	8.651	4.082	4.233	4.286	4.235
5	9	8.222	8.672	8.779	8.714	4.090	4.248	4.289	4.247
5	12	8.246	8.581	8.736	8.677	4.095	4.231	4.294	4.242
5	14	8.188	8.613	8.743	8.667	4.099	4.235	4.299	4.241
5	17	8.222	8.590	8.748	8.653	4.082	4.226	4.292	4.228

Table S6: Lattice constants value for $w_\sigma = 5$ set.

R_Ψ	R_n	a [Å]					c [Å]		
		{8,4,0}	{12,8,0}	{16,12,0}	{12,8,4}	{8,4,0}	{12,8,0}	{16,12,0}	{12,8,4}
3.2	6	8.577	8.910	8.952	8.928	4.240	4.358	4.366	4.350
3.2	9	8.625	8.946	8.971	8.966	4.265	4.346	4.356	4.338
3.2	12	8.611	8.948	8.972	8.965	4.259	4.345	4.356	4.339
3.2	14	8.609	8.950	8.973	8.966	4.258	4.346	4.356	4.339
3.2	17	8.607	8.950	8.972	8.965	4.257	4.345	4.356	4.339
3.6	6	8.586	8.911	8.952	8.929	4.249	4.361	4.368	4.352
3.6	9	8.633	8.951	8.971	8.968	4.269	4.348	4.360	4.339
3.6	12	8.623	8.956	8.986	8.974	4.267	4.348	4.355	4.345
3.6	14	8.618	8.957	8.977	8.975	4.262	4.346	4.356	4.339
3.6	17	8.620	8.964	8.984	8.988	4.262	4.344	4.355	4.337
4	6	8.595	8.913	8.955	8.948	4.257	4.362	4.370	4.347
4	9	8.633	8.950	8.974	8.967	4.273	4.349	4.359	4.342
4	12	8.623	8.966	8.991	8.987	4.265	4.347	4.353	4.343
4	14	8.621	8.957	8.980	8.973	4.267	4.349	4.358	4.341
4	17	8.614	8.957	8.977	8.976	4.260	4.343	4.353	4.335
4.4	6	8.605	8.914	8.953	8.954	4.265	4.366	4.373	4.350
4.4	9	8.634	8.961	8.993	8.978	4.273	4.352	4.358	4.344
4.4	12	8.624	8.959	8.986	8.981	4.266	4.345	4.352	4.337
4.4	14	8.625	8.965	8.978	8.988	4.268	4.343	4.356	4.335
4.4	17	8.614	8.960	8.982	8.979	4.259	4.349	4.355	4.340
4.7	6	8.613	8.915	8.955	8.957	4.270	4.365	4.373	4.348
4.7	9	8.636	8.960	8.989	8.979	4.275	4.351	4.358	4.347
4.7	12	8.622	8.960	8.980	8.978	4.268	4.349	4.358	4.340
4.7	14	8.626	8.961	8.985	8.984	4.270	4.347	4.356	4.335
4.7	17	8.629	8.973	8.992	9.002	4.262	4.346	4.356	4.335
5	6	8.610	8.901	8.960	8.930	4.268	4.363	4.369	4.355
5	9	8.637	8.973	9.003	8.989	4.271	4.352	4.360	4.347
5	12	8.629	8.963	8.982	8.987	4.275	4.347	4.358	4.336
5	14	8.627	8.973	8.992	8.995	4.268	4.345	4.359	4.336
5	17	8.620	8.976	8.992	9.000	4.261	4.345	4.352	4.335

Table S7: Lattice constants value for $w_\sigma = 10$ set.

R_Ψ	R_n	a [Å]					c [Å]		
		{8,4,0}	{12,8,0}	{16,12,0}	{12,8,4}	{8,4,0}	{12,8,0}	{16,12,0}	{12,8,4}
3.2	6	8.847	8.947	8.974	8.978	4.341	4.374	4.374	4.356
3.2	9	8.765	8.978	8.991	8.990	4.385	4.361	4.364	4.350
3.2	12	8.758	8.982	8.992	8.993	4.385	4.361	4.365	4.351
3.2	14	8.757	8.983	8.993	8.994	4.386	4.361	4.365	4.352
3.2	17	8.757	8.982	8.992	8.995	4.385	4.360	4.364	4.351
3.6	6	8.851	8.946	8.977	8.978	4.346	4.376	4.375	4.357
3.6	9	8.773	8.984	8.991	8.997	4.384	4.362	4.368	4.352
3.6	12	8.765	8.988	9.004	8.999	4.385	4.362	4.363	4.355
3.6	14	8.764	8.988	8.996	9.001	4.384	4.359	4.363	4.350
3.6	17	8.771	8.997	9.010	9.019	4.384	4.357	4.361	4.345
4	6	8.854	8.949	8.979	8.978	4.351	4.376	4.376	4.359
4	9	8.773	8.982	8.993	8.993	4.388	4.363	4.367	4.353
4	12	8.772	8.996	9.012	9.018	4.389	4.360	4.360	4.350
4	14	8.769	8.989	8.999	8.999	4.389	4.362	4.366	4.353
4	17	8.765	8.989	8.999	9.003	4.383	4.357	4.361	4.347
4.4	6	8.861	8.972	8.980	8.981	4.358	4.374	4.380	4.362
4.4	9	8.777	8.992	9.010	9.018	4.386	4.365	4.365	4.350
4.4	12	8.770	8.992	9.006	9.009	4.382	4.358	4.360	4.348
4.4	14	8.774	8.996	9.002	9.011	4.382	4.356	4.365	4.344
4.4	17	8.770	8.993	9.001	9.008	4.384	4.363	4.363	4.351
4.7	6	8.859	8.974	8.983	8.983	4.360	4.374	4.381	4.361
4.7	9	8.777	8.991	9.008	9.018	4.387	4.364	4.366	4.353
4.7	12	8.771	8.991	9.001	9.004	4.388	4.361	4.366	4.351
4.7	14	8.780	8.994	9.006	9.010	4.387	4.360	4.366	4.346
4.7	17	8.780	9.003	9.011	9.036	4.380	4.359	4.364	4.341
5	6	8.856	8.941	8.986	8.988	4.357	4.381	4.376	4.361
5	9	8.782	9.004	9.022	9.031	4.383	4.364	4.367	4.352
5	12	8.781	8.997	9.004	9.013	4.386	4.361	4.367	4.347
5	14	8.789	9.011	9.010	9.027	4.391	4.357	4.367	4.345
5	17	8.779	9.012	9.013	9.025	4.386	4.357	4.361	4.345

Table S8: Lattice constants value for $w_\sigma = 25$ set.

R_Ψ	R_n	a [Å]			c [Å]		
		{8,4,0}	{12,8,0}	{16,12,0}	{8,4,0}	{12,8,0}	{16,12,0}
3.2	6	8.960	9.004	9.005	4.472	4.384	4.389
3.2	9	8.843	9.008	9.015	4.489	4.379	4.381
3.2	12	9.020	9.013	9.016	4.404	4.378	4.381
3.2	14	9.020	9.013	9.016	4.404	4.377	4.381
3.2	17	9.021	9.013	9.016	4.401	4.377	4.380
3.6	6	8.961	9.003	9.004	4.468	4.386	4.391
3.6	9	8.852	9.015	9.014	4.484	4.378	4.384
3.6	12	9.021	9.030	9.024	4.401	4.374	4.380
3.6	14	9.020	9.018	9.019	4.399	4.373	4.379
3.6	17	9.028	9.030	9.029	4.398	4.371	4.377
4	6	8.964	9.004	9.005	4.462	4.387	4.392
4	9	8.854	9.025	9.017	4.481	4.376	4.382
4	12	9.028	9.030	9.030	4.404	4.373	4.376
4	14	9.026	9.030	9.023	4.404	4.374	4.381
4	17	9.022	9.021	9.020	4.399	4.373	4.378
4.4	6	8.967	9.004	9.005	4.457	4.390	4.395
4.4	9	8.859	9.030	9.025	4.479	4.377	4.382
4.4	12	8.852	9.029	9.025	4.480	4.372	4.377
4.4	14	9.028	9.026	9.024	4.396	4.371	4.381
4.4	17	9.032	9.023	9.019	4.398	4.377	4.380
4.7	6	8.963	9.006	9.007	4.451	4.389	4.396
4.7	9	8.858	9.031	9.026	4.479	4.375	4.382
4.7	12	9.028	9.032	9.024	4.403	4.373	4.381
4.7	14	9.035	9.032	9.024	4.399	4.372	4.382
4.7	17	9.035	9.037	9.026	4.393	4.370	4.379
5	6	8.964	9.005	9.009	4.440	4.388	4.392
5	9	9.033	9.041	9.034	4.400	4.374	4.383
5	12	9.035	9.033	9.024	4.398	4.373	4.382
5	14	9.046	9.038	9.027	4.399	4.371	4.380
5	17	9.041	9.037	9.029	4.397	4.372	4.377

Table S9: Lattice constants value for $w_\sigma = 50$ set.

R_Ψ	R_n	a [Å]			c [Å]		
		{8,4,0}	{12,8,0}	{16,12,0}	{8,4,0}	{12,8,0}	{16,12,0}
3.2	6	9.000	9.039	9.033	4.497	4.405	4.411
3.2	9	8.995	9.041	9.036	4.472	4.398	4.404
3.2	12	9.049	9.050	9.033	4.439	4.395	4.404
3.2	14	9.048	9.050	9.032	4.440	4.394	4.404
3.2	17	9.048	9.050	9.031	4.437	4.393	4.403
3.6	6	9.002	9.039	9.033	4.492	4.406	4.412
3.6	9	9.000	9.046	9.034	4.468	4.397	4.406
3.6	12	9.049	9.053	9.040	4.434	4.394	4.402
3.6	14	8.994	9.050	9.035	4.472	4.392	4.401
3.6	17	9.055	9.051	9.043	4.430	4.392	4.399
4	6	9.001	9.039	9.033	4.487	4.405	4.413
4	9	9.001	9.043	9.035	4.467	4.400	4.406
4	12	9.002	9.051	9.044	4.471	4.394	4.399
4	14	9.054	9.054	9.036	4.436	4.394	4.404
4	17	8.997	9.053	9.040	4.471	4.392	4.400
4.4	6	9.002	9.039	9.032	4.483	4.408	4.415
4.4	9	9.003	9.046	9.041	4.466	4.400	4.405
4.4	12	9.000	9.052	9.043	4.467	4.393	4.399
4.4	14	9.056	9.052	9.042	4.427	4.390	4.402
4.4	17	9.060	9.054	9.036	4.429	4.395	4.403
4.7	6	8.997	9.040	9.032	4.478	4.406	4.416
4.7	9	9.002	9.047	9.042	4.464	4.398	4.405
4.7	12	9.004	9.055	9.038	4.469	4.393	4.404
4.7	14	9.060	9.053	9.042	4.428	4.391	4.403
4.7	17	9.060	9.057	9.042	4.424	4.389	4.399
5	6	9.001	9.039	9.032	4.470	4.407	4.413
5	9	8.905	9.052	9.046	4.497	4.397	4.406
5	12	9.059	9.053	9.041	4.427	4.393	4.403
5	14	9.069	9.057	9.041	4.425	4.391	4.399
5	17	9.066	9.056	9.045	4.423	4.392	4.397

Bulk modulus

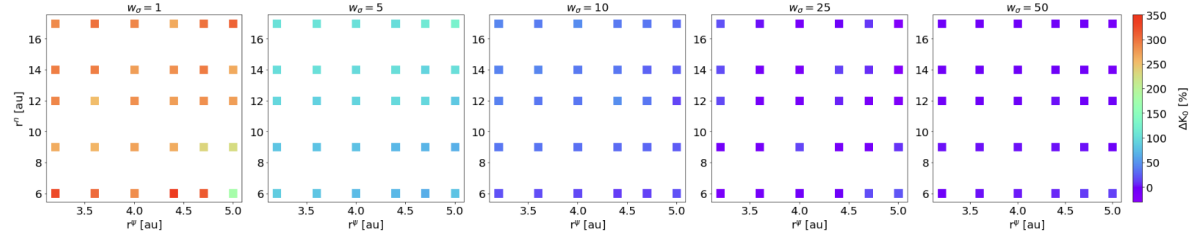


Figure S9: Percentage deviation from DFT bulk modulus of schreibersite for the $\{8,4,0\}$ set.

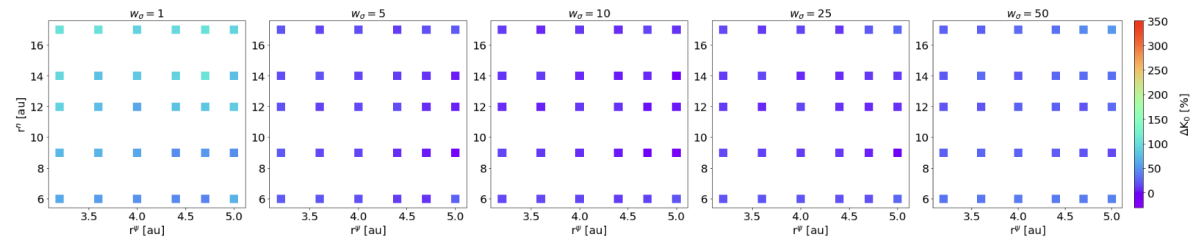


Figure S10: Percentage deviation from DFT bulk modulus of schreibersite for the $\{12,8,0\}$ set.

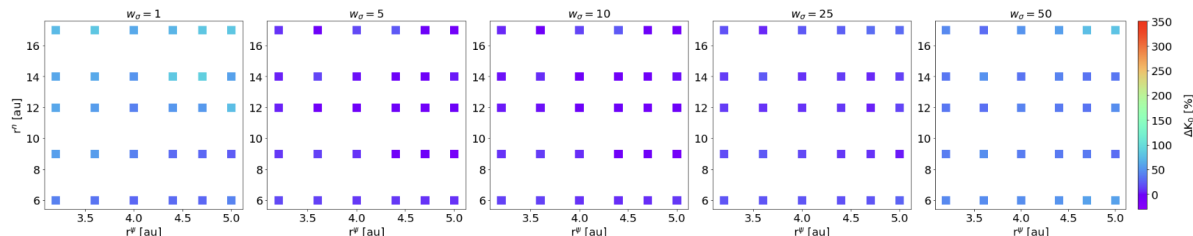


Figure S11: Percentage deviation from DFT bulk modulus of schreibersite for the $\{16,12,0\}$ set.

Table S10: Bulk modulus of schreibersite for the {8,4,0} set as a function of w_σ .

R_Ψ	R_n	$w_\sigma=0$	$w_\sigma=5$	$w_\sigma=10$	$w_\sigma=25$	$w_\sigma=50$
3.2	6	675.325	342.759	243.748	203.069	168.867
3.2	9	662.245	350.413	246.413	205.133	170.794
3.2	12	735.415	321.744	206.077	148.208	169.259
3.2	14	627.185	311.802	233.186	159.435	175.474
3.2	17	668.858	335.509	241.636	201.894	167.937
3.6	6	676.858	349.414	246.385	157.412	172.502
3.6	9	688.528	353.997	240.218	175.252	168.672
3.6	12	696.006	309.981	204.119	157.474	174.756
3.6	14	616.953	309.119	230.318	156.93	174.374
3.6	17	606.281	324.727	234.048	154.396	170.639
4	6	678.742	330.986	219.6	185.257	167.44
4	9	689.055	367.513	233.17	190.717	168.774
4	12	713.52	284.545	196.738	203.722	192.399
4	14	573.671	292.521	220.705	153.729	174.817
4	17	656.929	336.166	234.02	150.631	170.831
4.4	6	642.395	340.027	235.781	150.74	169.036
4.4	9	667.769	349.864	250.896	153.864	170.42
4.4	12	659.458	300.995	200.435	164.761	178.158
4.4	14	637.586	306.621	228.601	197.872	175.037
4.4	17	657.356	330.475	232.995	154.092	173.092
4.7	6	657.437	347.029	233.364	194.453	170.411
4.7	9	629.247	343.109	235.669	171.915	168.183
4.7	12	756.609	294.303	192.513	169.591	183.54
4.7	14	626.188	295.696	222.525	154.077	175.214
4.7	17	642.74	339.572	253.669	180.7	174.726
5	6	630.793	345.494	215.077	132.961	155.049
5	9	704.353	387.903	224.352	134.715	154.825
5	12	479.598	308.978	204.761	208.449	195.071
5	14	563.202	287.916	212.805	188.023	172.169
5	17	641.292	316.81	197.466	139.63	171.892

Table S11: Bulk modulus of schreibersite for the {12,8,0} set as a function of w_σ .

R_Ψ	R_n	$w_\sigma=0$	$w_\sigma=5$	$w_\sigma=10$	$w_\sigma=25$	$w_\sigma=50$
3.2	6	337.127	204.39	189.112	194.282	212.12
3.2	9	351.534	209.17	193.049	200.285	215.157
3.2	12	281.093	212.717	201.052	207.38	231.889
3.2	14	294.69	211.785	197.587	200.669	217.166
3.2	17	326.733	204.756	186.566	192.311	209.663
3.6	6	305.802	207.806	192.943	200.661	224.283
3.6	9	351.242	198.063	183.487	190.411	214.892
3.6	12	267.131	209.717	199.685	208.94	233.316
3.6	14	292.685	201.877	189.385	196.483	220.135
3.6	17	302.218	196.867	180.646	183.137	209.437
4	6	353.376	187.784	182.052	190.908	225.89
4	9	351.782	207.044	199.036	212.209	249.162
4	12	245.048	187.762	196.091	206.18	238.49
4	14	263.632	178.359	170.478	181.312	208.045
4	17	310.676	186.559	175.534	182.324	209.66
4.4	6	316.693	197.139	182.133	184.039	210.968
4.4	9	328.699	202.955	191.813	197.563	224.648
4.4	12	257.153	205.793	197.542	207.88	235.483
4.4	14	276.699	198.571	186.425	194.256	218.154
4.4	17	277.265	200.811	190.091	198.148	219.259
4.7	6	328.308	194.293	178.705	186.03	221.904
4.7	9	339.171	192.861	185.148	190.508	227.909
4.7	12	250.206	192.34	193.748	206.294	237.234
4.7	14	251.466	185.405	178.139	190.712	213.043
4.7	17	308.688	204.342	188.687	189.028	215.767
5	6	302.367	178.839	167.568	192.761	228.907
5	9	330.202	210.378	187.4	222.454	263.161
5	12	289.726	219.09	208.299	221.526	242.313
5	14	253.627	160.287	155.322	170.36	200.064
5	17	320.484	180.204	177.201	187.181	224.999

Table S12: Bulk modulus of schreibersite for the {16,12,0} set as a function of w_σ .

R_Ψ	R_n	$w_\sigma=0$	$w_\sigma=5$	$w_\sigma=10$	$w_\sigma=25$	$w_\sigma=50$
3.2	6	278.367	179.738	176.408	193.048	235.029
3.2	9	298.102	188.971	183.177	205.919	249.298
3.2	12	242.182	199.74	195.941	208.37	250.515
3.2	14	270.87	190.439	188.985	204.434	240.15
3.2	17	278.236	180.764	178.578	192.903	234.697
3.6	6	279.065	198.279	185.1	210.763	257.353
3.6	9	313.904	172.37	171.34	182.839	225.092
3.6	12	232.561	196.702	196.509	208.256	253.08
3.6	14	265.98	194.459	192.419	209.99	254.704
3.6	17	266.123	167.298	175.573	188.783	228.265
4	6	322.085	168.912	168.198	183.106	232.675
4	9	312.148	172.091	171.978	226.23	302.534
4	12	219.97	187.23	185.52	209.309	273.473
4	14	221.408	169.246	170.565	188.314	235.594
4	17	265.857	164.756	165.463	180.331	231.236
4.4	6	259.687	174.152	171.083	187.91	230.364
4.4	9	279.183	201.328	197.177	211.908	258.259
4.4	12	221.352	189.336	187.227	207.595	255.551
4.4	14	241.344	188.903	185.143	199.574	239.515
4.4	17	242.765	170.955	173.666	187.656	243.19
4.7	6	315.605	171.605	168.718	194.079	244.603
4.7	9	292.406	211.501	170.265	216.666	270.317
4.7	12	222.668	189.622	186.483	205.991	259.303
4.7	14	222.538	166.389	167.246	191.129	235.426
4.7	17	261.451	171.603	171.824	191.422	236.177
5	6	271.833	176.688	175.946	194.989	235.05
5	9	312.826	162.262	161.987	223.132	308.649
5	12	245.196	188.068	190.031	217.764	272.059
5	14	214.466	155.482	156.69	178.41	225.836
5	17	301.875	172.874	172.923	197.658	253.147

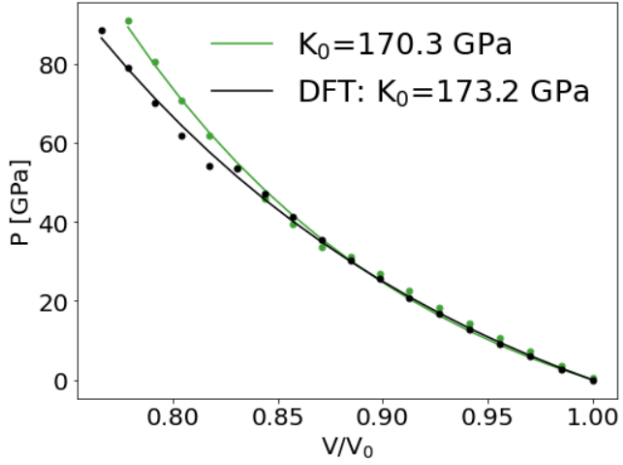


Figure S12: Cold curve for the DFT and DFTB/ChIMES $R_\Psi = 4.7$ au, $R_n = 9.0$ au $\{16, 12, 0\}/w_\sigma = 10$ parametrization.

Surface formation energy

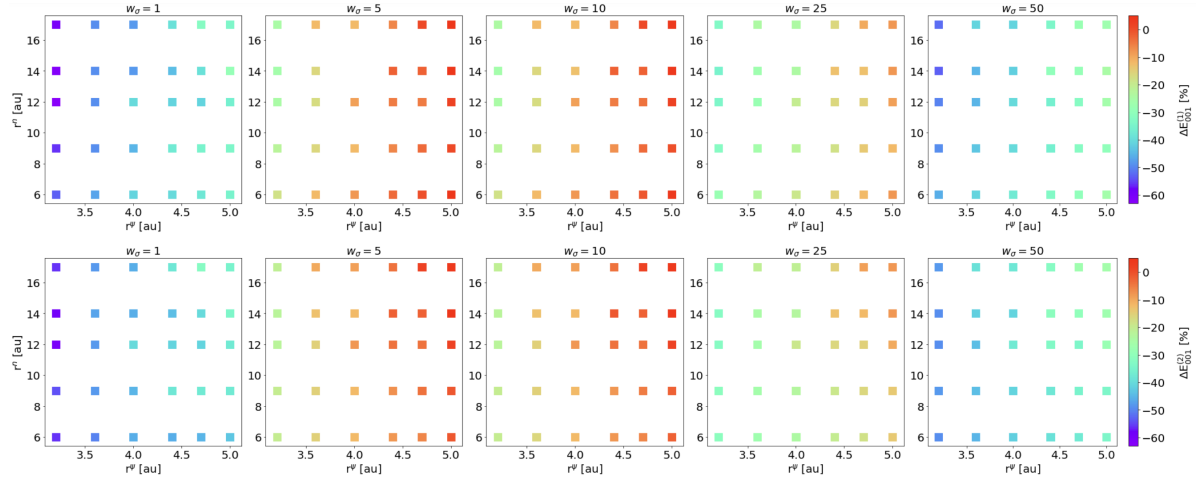


Figure S13: Percentage deviation from DFT surface formation energy for (001) surface for $R_\Psi = 4.7$ au, $R_n = 9.0$ au $\{16, 12, 0\}$ parametrization, as a function of w_σ .

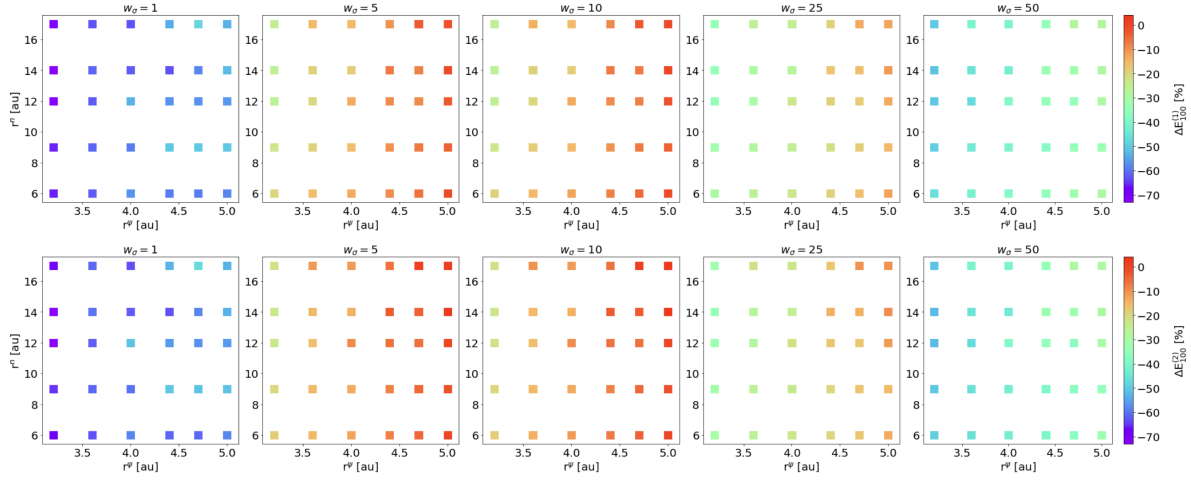


Figure S14: Percentage deviation from DFT surface formation energy for (100) surface for $R_\Psi = 4.7$ au, $R_n = 9.0$ au $\{16, 12, 0\}$ parametrization, as a function of w_σ .

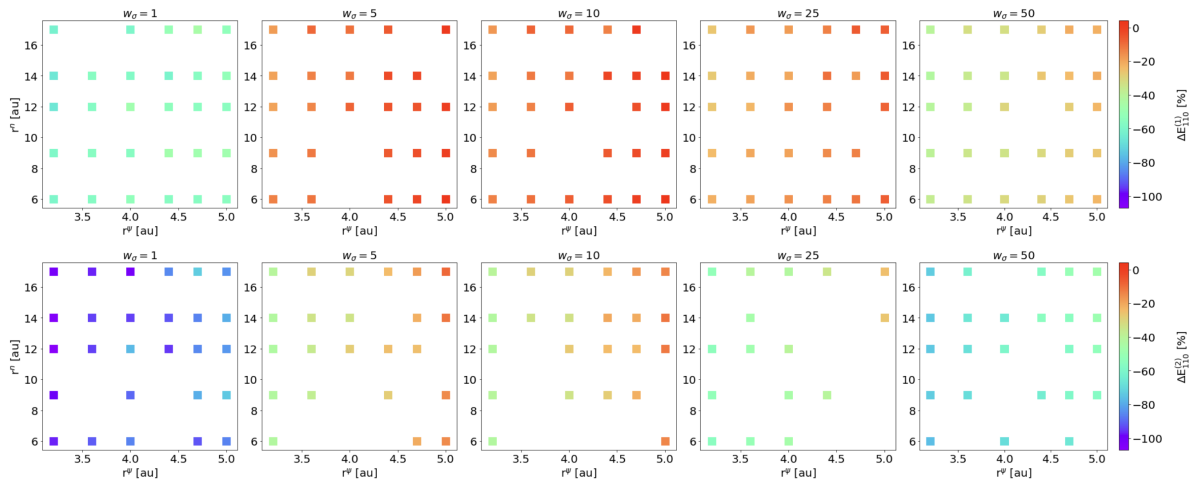


Figure S15: Percentage deviation from DFT surface formation energy for (110) surface for $R_\Psi = 4.7$ au, $R_n = 9.0$ au $\{16, 12, 0\}$ parametrization, as a function of w_σ .

Table S13: Surface formation energy E_{surface} for $\{16, 12, 0\}/w_\sigma = 1$ set. Energies are reported in J/m^2 . Zero values correspond to non-converged runs thus to missing data in the previous plots.

R_Ψ	R_n	$E_{001}^{(1)}$	$E_{001}^{(2)}$	$E_{100}^{(1)}$	$E_{100}^{(2)}$	$E_{110}^{(1)}$	$E_{110}^{(2)}$
3.2	6	3.44	3.12	3.39	3.25	4.04	3.03
3.2	9	3.49	3.09	3.39	3.22	4.02	3.05
3.2	12	3.66	3.2	3.55	3.38	4.21	3.18
3.2	14	3.64	3.18	3.54	3.35	4.19	3.16
3.2	17	3.59	3.13	3.48	3.27	4.1	3.09
3.6	6	3.29	3.01	3.31	3.17	3.97	2.94
3.6	9	3.34	2.97	3.3	3.14	3.94	0
3.6	12	3.34	2.97	3.32	3.15	3.98	2.98
3.6	14	3.34	2.94	3.3	3.11	3.95	2.98
3.6	17	3.34	2.96	3.34	3.14	0	3.04
4	6	3.15	2.92	3.21	3.08	3.87	2.86
4	9	3.25	2.91	3.26	3.11	3.94	2.92
4	12	3.14	2.8	3.14	2.95	3.75	2.73
4	14	3.32	2.93	3.31	3.15	4	2.98
4	17	3.32	2.93	3.34	3.17	4.05	3.1
4.4	6	3.13	2.92	3.26	3.13	3.95	0
4.4	9	3.06	2.76	3.07	2.92	3.71	0
4.4	12	3.15	2.83	3.21	3.04	3.9	3
4.4	14	3.23	2.88	3.34	3.17	4.07	2.95
4.4	17	3.11	2.76	3.15	2.98	3.82	2.85
4.7	6	3.09	2.91	3.26	3.13	3.95	2.96
4.7	9	3.03	2.75	3.08	2.94	3.75	2.75
4.7	12	3.15	2.82	3.22	3.07	3.93	2.85
4.7	14	3.11	2.8	3.23	3.08	3.95	2.87
4.7	17	2.96	2.65	3.03	2.87	3.68	2.67
5	6	3.02	2.87	3.23	3.08	3.92	2.87
5	9	3.01	2.74	3.07	2.94	3.75	2.68
5	12	3.05	2.75	3.19	3.05	3.92	2.82
5	14	2.89	2.69	3.12	2.98	3.85	2.75
5	17	3	2.71	3.13	2.98	3.88	2.84

Table S14: Surface formation energy E_{surface} for $\{16, 12, 0\}/w_\sigma = 5$ set. Energies are reported in J/m^2 . Zero values correspond to non-converged runs thus to missing data in the previous plots.

R_Ψ	R_n	$E_{001}^{(1)}$	$E_{001}^{(2)}$	$E_{100}^{(1)}$	$E_{100}^{(2)}$	$E_{110}^{(1)}$	$E_{110}^{(2)}$
3.2	6	2.64	2.4	2.46	2.31	2.87	2.19
3.2	9	2.74	2.41	2.52	2.34	2.93	2.18
3.2	12	2.8	2.44	2.57	2.39	3	2.2
3.2	14	2.82	2.44	2.58	2.4	3.01	2.19
3.2	17	2.8	2.42	2.56	2.38	2.99	2.17
3.6	6	2.51	2.31	2.38	2.24	2.8	0
3.6	9	2.59	2.3	2.43	2.25	2.84	2.12
3.6	12	2.62	2.3	2.46	2.27	2.88	2.09
3.6	14	2.6	2.27	2.44	2.24	2.86	2.07
3.6	17	2.52	2.21	2.36	2.16	2.75	1.99
4	6	2.42	2.25	2.31	2.18	0	0
4	9	2.52	2.24	2.37	2.21	0	0
4	12	2.44	2.16	2.31	2.12	2.72	1.97
4	14	0	2.25	2.42	2.23	2.84	2.06
4	17	2.51	2.18	2.36	2.17	2.78	2
4.4	6	2.32	2.17	2.23	2.1	2.65	0
4.4	9	2.38	2.15	2.26	2.11	2.68	1.97
4.4	12	2.35	2.09	2.24	2.06	2.65	1.92
4.4	14	2.29	2.04	2.19	2.01	2.6	0
4.4	17	2.37	2.08	2.25	2.07	2.67	1.91
4.7	6	2.25	2.12	2.17	2.05	2.58	1.86
4.7	9	2.31	2.09	2.2	2.05	2.62	0
4.7	12	2.35	2.09	2.23	2.07	2.66	1.93
4.7	14	2.29	2.04	2.21	2.02	2.59	1.88
4.7	17	2.22	1.96	2.11	1.93	0	1.81
5	6	2.14	2.03	2.07	1.95	2.45	1.77
5	9	2.23	2.03	2.12	1.98	2.53	1.77
5	12	2.2	1.97	2.11	1.95	2.52	0
5	14	2.14	1.91	2.06	1.89	0	1.71
5	17	2.14	1.92	2.08	1.91	2.49	1.68

Table S15: Surface formation energy E_{surface} for $\{16, 12, 0\}/w_\sigma = 10$ set. Energies are reported in J/m^2 . Zero values correspond to non-converged runs thus to missing data in the previous plots.

R_Ψ	R_n	$E_{001}^{(1)}$	$E_{001}^{(2)}$	$E_{100}^{(1)}$	$E_{100}^{(2)}$	$E_{110}^{(1)}$	$E_{110}^{(2)}$
3.2	6	2.64	2.4	2.44	2.3	2.85	2.18
3.2	9	2.74	2.41	2.51	2.34	2.92	2.17
3.2	12	2.8	2.44	2.56	2.38	2.98	2.18
3.2	14	2.82	2.44	2.57	2.39	3	2.18
3.2	17	2.77	2.42	2.55	2.37	2.97	2.16
3.6	6	2.51	2.32	2.36	2.23	2.78	0
3.6	9	2.59	2.31	2.42	2.25	2.82	0
3.6	12	2.62	2.31	2.45	2.27	2.87	0
3.6	14	2.6	2.27	2.43	2.24	2.84	2.06
3.6	17	2.52	2.2	2.34	2.15	2.73	1.99
4	6	2.42	2.25	2.29	2.17	2.71	0
4	9	2.5	2.25	2.36	2.2	0	2.07
4	12	2.45	2.17	2.31	2.12	2.71	1.96
4	14	2.54	2.25	2.41	2.22	2.83	2.05
4	17	2.51	2.19	2.35	2.16	2.76	1.99
4.4	6	2.33	2.17	2.21	2.09	2.62	0
4.4	9	2.39	2.16	2.26	2.11	2.67	1.97
4.4	12	2.35	2.09	2.23	2.06	0	1.91
4.4	14	2.29	2.03	2.18	2	2.57	1.85
4.4	17	2.37	2.08	2.24	2.06	2.85	1.89
4.7	6	2.26	2.12	2.14	2.03	2.54	0
4.7	9	2.32	2.1	2.2	2.05	2.61	1.88
4.7	12	2.33	2.09	2.22	2.06	2.63	1.91
4.7	14	2.29	2.04	2.19	2.01	2.56	1.86
4.7	17	2.23	1.97	2.1	1.93	2.47	1.8
5	6	2.15	2.04	2.06	1.94	2.42	1.76
5	9	2.24	2.04	2.12	1.98	2.52	0
5	12	2.2	1.97	2.09	1.94	2.49	1.72
5	14	2.15	1.92	2.05	1.88	2.43	1.71
5	17	2.16	1.93	2.07	1.9	0	1.76

Table S16: Surface formation energy E_{surface} for $\{16, 12, 0\}/w_\sigma = 25$ set. Energies are reported in J/m^2 . Zero values correspond to non-converged runs thus to missing data in the previous plots.

R_Ψ	R_n	$E_{001}^{(1)}$	$E_{001}^{(2)}$	$E_{100}^{(1)}$	$E_{100}^{(2)}$	$E_{110}^{(1)}$	$E_{110}^{(2)}$
3.2	6	2.88	2.63	2.65	2.53	3.08	2.39
3.2	9	2.96	2.62	2.71	2.56	3.14	2.34
3.2	12	3.01	2.65	2.76	2.6	3.2	2.37
3.2	14	3.02	2.65	2.77	2.61	3.22	0
3.2	17	2.99	2.62	2.74	2.58	3.18	2.34
3.6	6	2.76	2.55	2.57	2.46	3.02	2.33
3.6	9	2.82	2.52	2.62	2.46	3.04	0
3.6	12	2.86	2.53	2.66	2.5	3.1	2.28
3.6	14	2.85	2.5	2.64	2.47	3.07	2.25
3.6	17	2.77	2.42	2.55	2.37	2.96	2.17
4	6	2.67	2.49	2.51	2.4	2.94	2.25
4	9	2.74	2.47	2.56	2.42	3	2.23
4	12	2.7	2.39	2.52	2.35	2.93	2.15
4	14	2.77	2.47	2.6	2.44	3.04	0
4	17	2.77	2.42	2.56	2.39	2.99	2.18
4.4	6	2.57	2.41	2.43	2.33	2.87	0
4.4	9	2.64	2.39	2.47	2.34	2.9	2.17
4.4	12	2.6	2.32	2.43	2.28	2.86	0
4.4	14	2.54	2.26	2.39	2.22	2.79	0
4.4	17	2.6	2.3	2.44	2.28	2.87	2.08
4.7	6	2.51	2.37	2.37	2.28	2.8	0
4.7	9	2.56	2.33	2.41	2.28	2.85	0
4.7	12	2.57	2.31	2.42	2.28	0	0
4.7	14	2.53	2.25	2.38	2.22	2.98	0
4.7	17	2.47	2.19	2.31	2.15	2.69	0
5	6	2.42	2.29	2.3	2.2	2.71	0
5	9	2.5	2.29	2.36	2.24	0	0
5	12	2.44	2.2	2.31	2.17	2.72	0
5	14	2.42	2.16	2.27	2.12	2.67	1.94
5	17	2.42	2.16	2.29	2.14	2.7	1.92

Table S17: Surface formation energy E_{surface} for $\{16, 12, 0\}/w_\sigma = 50$ set. Energies are reported in J/m^2 . Zero values correspond to non-converged runs thus to missing data in the previous plots.

R_Ψ	R_n	$E_{001}^{(1)}$	$E_{001}^{(2)}$	$E_{100}^{(1)}$	$E_{100}^{(2)}$	$E_{110}^{(1)}$	$E_{110}^{(2)}$
3.2	6	3.27	2.99	2.99	2.91	3.47	2.71
3.2	9	3.34	2.97	3.05	2.93	3.52	2.66
3.2	12	3.37	2.99	3.08	2.96	3.56	2.68
3.2	14	3.43	2.99	3.09	2.97	3.58	2.68
3.2	17	3.4	2.97	3.07	2.94	3.55	2.66
3.6	6	3.16	2.91	2.91	2.84	3.39	0
3.6	9	3.21	2.88	2.95	2.84	3.42	2.6
3.6	12	3.24	2.88	3	2.86	3.47	2.59
3.6	14	3.26	2.85	2.97	2.83	3.44	2.56
3.6	17	3.17	2.78	2.88	2.74	3.33	2.49
4	6	3.06	2.85	2.84	2.78	3.32	2.6
4	9	3.13	2.82	2.89	2.79	3.38	0
4	12	3.13	2.74	2.84	2.71	3.3	2.47
4	14	3.19	2.82	2.92	2.81	3.42	2.54
4	17	3.16	2.77	2.88	2.75	3.35	0
4.4	6	2.98	2.79	2.78	2.72	3.26	0
4.4	9	3.05	2.77	2.82	2.73	3.31	2.52
4.4	12	3.05	2.67	2.76	2.64	0	0
4.4	14	2.92	2.63	2.72	2.6	3.18	2.38
4.4	17	3	2.65	2.77	2.64	3.23	2.41
4.7	6	2.91	2.74	2.72	2.67	3.19	2.56
4.7	9	2.97	2.71	2.76	2.68	3.25	2.45
4.7	12	2.97	2.68	2.77	2.67	3.25	2.44
4.7	14	2.89	2.61	2.71	2.58	3.14	2.38
4.7	17	2.88	2.54	2.63	2.5	3.06	2.32
5	6	2.83	2.68	2.65	2.59	3.11	0
5	9	2.92	2.68	2.72	2.64	3.2	2.41
5	12	2.83	2.57	2.64	2.54	3.1	2.35
5	14	2.81	2.54	2.62	2.51	3.07	2.3
5	17	2.85	2.53	2.62	2.51	3.08	2.27

Bulk interstitial water absorption

Table S18: Bulk water absorption energies $\{16, 12, 0\}$ set obtained for both interstitial sites and for $w_\sigma = 5$ and $w_\sigma = 10$. Zero values correspond to non-converged runs thus to missing data in the plots in the main text.

R_Ψ	R_n	$w_\sigma=5$		$w_\sigma=10$	
		Site 1	Site 2	Site 1	Site 2
3.2	6	-2.17	-1.88	-2.15	-1.84
3.2	9	-2.28	-1.99	-2.25	-1.94
3.2	12	-2.35	-2.06	-2.33	-2.01
3.2	14	-1.07	-0.97	-1.05	-0.92
3.2	17	-1.86	-1.56	-1.86	-1.52
3.6	6	-2.54	-2.16	-2.49	-2.09
3.6	9	-2.63	-2.22	-2.61	-2.18
3.6	12	-2.69	-2.3	-2.68	-2.23
3.6	14	-1.57	-1.59	-1.55	-1.54
3.6	17	-2.2	-1.87	-2.19	-1.82
4	6	-2.94	-2.47	-2.93	-2.4
4	9	-3.02	-2.57	-3.01	-2.53
4	12	-3.09	-2.62	-3.11	-2.59
4	14	-2.08	-2.23	-2.06	-2.17
4	17	-2.62	-2.22	-2.59	-2.17
4.4	6	-3.38	-2.85	-3.37	-2.79
4.4	9	-3.5	-2.99	-3.48	-2.92
4.4	12	-3.5	-3	-3.52	-2.98
4.4	14	-2.55	-2.79	-2.53	-2.74
4.4	17	-3.03	-2.61	-2.99	-2.54
4.7	6	-3.66	-3.16	-3.64	-3.1
4.7	9	-3.79	-3.27	-3.78	-3.22
4.7	12	-3.87	-3.36	-3.86	-3.31
4.7	14	-2.86	-3.18	-2.84	-3.12
4.7	17	-3.34	-2.88	-3.29	-2.81
5	6	-4	-3.45	-3.99	-3.39
5	9	-4.07	-3.55	0	0
5	12	-4.21	-3.65	0	0
5	14	-3.15	-3.53	0	0
5	17	-3.62	-3.16	0	0